Journal of Volcanology and Geothermal Research 387 (2019) 106665

Contents lists available at ScienceDirect

Journal of Volcanology and Geothermal Research

journal homepage: www.elsevier.com/locate/jvolgeores

Understanding melt evolution and eruption dynamics of the 1666 C.E. eruption of Cinder Cone, Lassen Volcanic National Park, California: Insights from olivine-hosted melt inclusions

K.J. Walowski[a,b,*], P.J. Wallace[b], K.V. Cashman[c], J.K. Marks[b], M.A. Clynne[d], P. Ruprecht[e]

[a] Middlebury College, Department of Geology, Middlebury, VT 05753, USA
[b] University of Oregon, Department of Earth Sciences, Eugene, OR 97403, USA
[c] University of Bristol, Department of Earth Sciences, Bristol, United Kingdom
[d] United States Geological Survey, Volcano Science Center, Menlo Park, CA, USA
[e] University of Nevada, Reno, NV, USA

ARTICLE INFO

Article history:
Received 1 February 2019
Received in revised form 15 August 2019
Accepted 19 August 2019
Available online 27 August 2019

Keywords:
Cinder cone
Scoria cone
Melt inclusions
Geochemistry
Tephra
Lassen
Magma
Volcano

ABSTRACT

Cinder Cone is the youngest scoria cone volcano in the continental United States. Erupted in 1666 C.E. within what is now Lassen Volcanic National Park, Cinder Cone is an un-vegetated scoria cone with well-preserved lava flows and tephra deposits that display complex geochemical variability. In this study, we utilize the volatile (H_2O, CO_2, Cl), major, and trace element chemistry of olivine-hosted melt inclusions from the tephra deposit of Cinder Cone to better understand the sub-surface evolution of magmas that erupt to produce scoria cones. High-Fo olivine phenocrysts from all erupted units contain melt inclusions that are more primitive in composition than the erupted material. The evolved compositions of the lava and bulk tephra and the abundance of quartz xenocrysts within the deposits suggest the basaltic parental magmas were rapidly contaminated by granitic material in the middle to upper crust, after melt inclusion entrapment. Distinct compositional variability between early and late erupted units suggests two different mantle-derived basaltic magmas were tapped and erupted sequentially as two distinct eruptive phases. The CO_2 concentrations in the melt inclusions, after correction for the presence of vapor bubbles, suggest minimum entrapment depths of ~9.5–20 km and show no resolvable differences between early and late erupted units at the time of olivine crystallization. Diffusion modeling of Ni and Fo gradients in olivine rims indicates that olivine residence times in an evolving magma were on the order of weeks to years, similar to those calculated for longer-lived scoria cone eruptions, such as Jorullo, in Mexico. Additionally, geochemical evidence suggests that the evolution of parental magmas was likely driven by the partial melting, disaggregation, and assimilation of granitic material in the upper crust. Our combined results provide new insight into the complexities of short-lived monogenetic eruptions.

1. Introduction

Scoria cone volcanoes are the most abundant subaerial volcanic landforms on Earth (Wood, 1980). In the Cascade Arc, they are typically mafic, and have been previously exploited to study mantle processes such as arc magma genesis (e.g., Borg et al., 1997, 2002; Leeman et al., 2004; Ruscitto et al., 2010; Walowski et al., 2015, 2016). The eruptions of scoria cones typically last weeks, months or years; as a result of these short timescales eruptions commonly involve a limited range of magma compositions. Some longer-lived scoria cones, however, produce evolved compositions that suggest the development of complex subvolcanic plumbing systems. At Parícutin, Mexico, for example, magmas evolved from basalt to andesite over the course of an eruption that lasted ~9 years (Wilcox, 1954; McBirney et al., 1987; Luhr and Carmichael, 1985; Luhr, 2001; Erlund et al., 2010). This compositional evolution was accompanied by a decrease in both explosivity and magmatic volatile contents, providing insight into shallow storage reservoirs beneath cones in central Mexico (Pioli et al., 2008; Johnson et al., 2008; Rowe et al., 2011).

At Cinder Cone, in Lassen Volcanic National Park, CA, the compositions of the erupted magmas also changed over the course of the eruption, although these changes are not systematic as observed at Parícutin (Clynne et al., 2000). The eruptive history of Cinder Cone can be summarized by three key observations: (1) The eruption

* Corresponding author at: Middlebury College, Department of Geology, Middlebury, VT 05753, USA.
E-mail address: kwalowski@middlebury.edu (K.J. Walowski).

https://doi.org/10.1016/j.jvolgeores.2019.106665
0377-0273/

was likely short (<5 years; Sheppard et al., 2009), (2) the eruption involved two main phases of explosive activity which differ in style and intensity, both accompanied by lava flows (Heiken, 1978; Marks, 2012), and (3) the erupted materials are ubiquitously contaminated by crustal rocks of granitic composition (Clynne and Muffler, 2010). What are the timescales associated with the storage and ascent of these magmas? With a complicated inter-fingering of tephra and lava flows, can we connect pre-eruptive changes in magma chemistry to changes in eruption dynamics? How does the potential crustal contamination occur?

To investigate these questions, we analyzed the compositions of olivine-hosted melt inclusions (MI) sampled from the entire eruptive sequence at Cinder Cone and their primitive olivine hosts. Melt inclusions are small volumes of melt trapped inside phenocrysts at depth, and as such, they can provide unique insights that extend interpretations based on traditional methods of bulk rock and mineral chemistry. Melt inclusions trapped in early crystallizing phases, such as olivine, can provide snapshots of melt chemistry before additional magmatic evolution by fractional crystallization, mixing, and/or contamination. In this way, MI may constrain parental melt compositions and magma generation, storage, and evolution. Melt inclusions also provide estimates of pre-eruptive concentrations of volatiles such as H_2O, CO_2, S, Cl (e.g., Métrich and Wallace, 2008) that are key to understanding mantle melting (Gaetani and Grove, 1998; Grove et al., 2006; Hirschmann et al., 2009) and magma ascent and eruption (e.g., Roggensack et al., 1997; Métrich and Wallace, 2008). Magmatic volatile contents are difficult to measure directly because they decrease in solubility as pressure decreases and therefore degas from the magma before or during ascent, driving eruptions, and leaving the erupted material with only a fraction of the volatile contents with which it began (Holloway and Blank, 1994). Melt inclusions are one of the best tools currently available to directly measure pre-eruptive volatile concentrations, because they are trapped at depth, often before significant degassing occurs. Because the solubility of H_2O and CO_2 in magmas is sensitive to pressure and experimentally well-constrained (Newman and Lowenstern, 2002; Papale et al., 2006; Iacono-Marziano et al., 2012; Ghiorso and Gualda, 2015), their concentrations within MI can provide estimates of entrapment pressures, and therefore, magma storage depths (e.g., Johnson et al., 2008; Pioli et al., 2008). Although recent work has shown that MI are not perfect storage containers and can lose H^+ (protons) by diffusion through the host and CO_2 due to formation of a vapor bubble in the inclusion post entrapment, there are methods for distinguishing and correcting for these effects (e.g., Bucholz et al., 2013; Lloyd et al., 2013; Moore et al., 2014; Wallace et al., 2015; Aster et al., 2016).

The primitive olivine hosts also keep a record of deep and early magma evolution. Trace element compositions in high-Fo olivine can be indicative of crystal fractionation prior to significant crustal involvement and may also track source variations in the mantle (e.g., Sobolev et al., 2005; Le Roux et al., 2011; Straub et al., 2011; Ruprecht and Plank, 2013). In addition, studies on the diffusivity of major and trace elements in olivine have shown the phase's utility to record the timescales of magmatic processes operating over months to decades (e.g. Petry et al., 2004; Dohmen and Chakraborty, 2007; Costa and Morgan, 2011). Thus, the information provided by the olivine hosts complements constraints from the MI record to develop an integrated spatial-temporal view of the magma plumbing system.

In this study, we analyze major, trace, and volatile element concentrations in olivine-hosted MI and their crystal hosts from the tephra deposit at Cinder Cone and provide a comparison to lava and bulk tephra compositions and olivine major and trace element chemistry. We interpret the data in the context of stratigraphic relationships between lava and tephra and textural analyses of tephra clasts (Marks, 2012). We use these results to shed light on the processes that led to compositional evolution of the magmas and accompanying changes in eruptive dynamics. We show that the volatile contents of MI can provide insight into the minimum depths at which these magmatic processes occur. We also demonstrate the usefulness of MI for determining the composition of the mantle source, even when the erupted magma is contaminated by crustal material. Lastly, we compare olivine residence and eruption timescales. Together these results allow us to construct a spatial-temporal schematic model for the plumbing system that fed the eruption of Cinder Cone. The combined results provide new insights on the complexities and mechanisms that drive scoria cone eruptions, and will help to better inform future hazard models of scoria cone-dominated volcanic fields globally.

2. Geologic setting

Cinder Cone is a basaltic andesite scoria cone located in the northeast corner of Lassen Volcanic National Park, northern California (Fig. 1). The tallest point in the park is Lassen Peak, a dacite dome complex that last erupted from 1914 to 1917 (Clynne and Muffler, 2010). Tectonically, volcanism within the Lassen Segment of the Cascades is caused by oblique subduction of the Gorda microplate beneath the North American plate, and is characterized by abundant calc-alkaline magmas (e.g., Clynne and Muffler, 2010). Tholeiitic magmas are also common in this region, however, and are often associated with extensional faulting, the result of westward expansion of the Basin and Range province impinging on the southern Cascade arc. The Quaternary volcanics in the Lassen region sit on top of older mafic to intermediate volcanoes and volcanic products 2–4 km thick (Berge and Stauber, 1987). This volcanic basement is underlain by plutonic Sierran and metamorphic Klamath terrain basement rocks, as suggested by mapped outcropping units (e.g. Saleeby et al., 1989; Cecil et al., 2012) and constant modeled seismic velocities across the Sierra Nevada-Cascade Range boundary (Berge and Stauber, 1987).

The eruption date of 1666 CE was established by dendrochemistry and ring-width analyses of living trees (Sheppard et al., 2009) which supported initial ages constrained by radiocarbon dates of trees killed by the lava flows (1650 ± 20 years; Clynne et al., 2000). At approximately 350 years old, it is the youngest scoria cone in the Cascade Arc; it has remained un-vegetated and thus provides excellent exposure of the lava flows and tephra deposit (Clynne and Muffler, 2010). The eruptive material comprises a ~200-m-tall scoria cone, a tephra deposit ≤3 m in thickness that covers an area of ~200 km^2, and five lava flows separated into three phases – Old Bench, Painted Dunes, and Fantastic Lava (OB, PD, and FL, respectively; Clynne and Muffler, 2010; Fig. 1).

3. Sample descriptions and tephra stratigraphy

The tephra deposit was first described in detail by Heiken (1978) who identified three eruptive phases that produced tephra Units 1, 2, and 3, which, based on geochemical data (Clynne, 2011), are now thought to correspond with the three phases of lava flow emplacement, OB, PD, and FL, respectively. This previous work supports 3 cycles of compositional evolution at Cinder Cone, one associated with each of the lava flow and tephra unit. Unit 1 is the least widespread, rare and difficult to identify, and associated with the least voluminous lava flow: OB. It is difficult to determine whether the unit was volumetrically insignificant, experienced erosion (the original interpretation of Heiken, 1978), or both. Unit 3 is the most voluminous and widespread of the three tephra units.

Tephra samples used in this study were collected from a ~1.2-m-deep pit to the north of Cinder Cone that includes the volumetrically

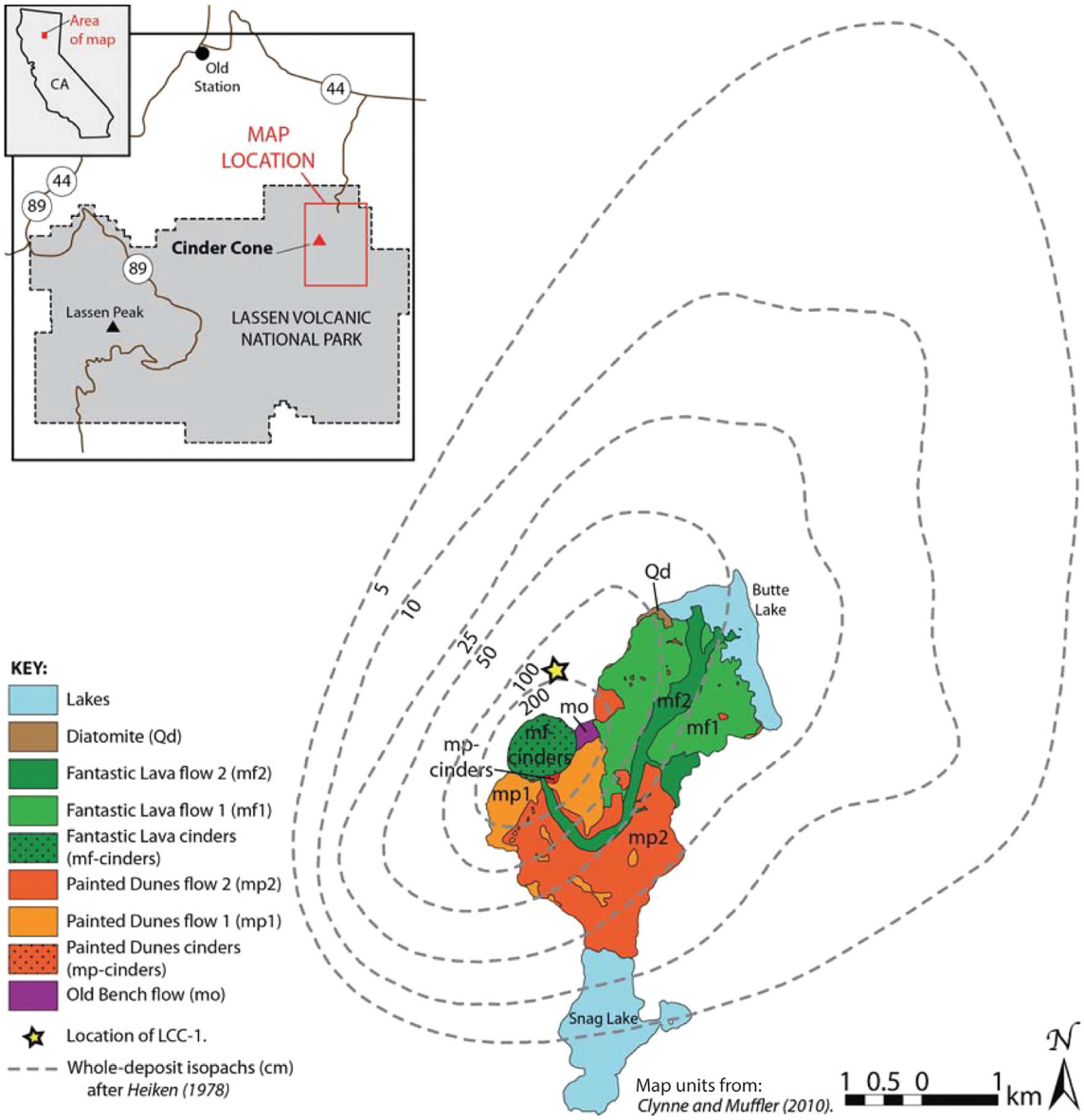

Fig. 1. Geologic (adapted from Clynne and Muffler, 2010) and isopach map (Heiken, 1978) of Cinder Cone showing the location of the cone, lava flows, and the whole-deposit tephra deposits. The location of the main tephra pit from which tephra was sampled for this study (LCC-1) is indicated by the yellow star. The legend shows geologic units in order of emplacement (i.e., Old Bench lavas being the oldest, and thus, at the base of the section). The three main lava flows are colored Purple = Old Bench (OB; tephra Unit 1), orange = Painted Dunes (PD; tephra Unit 2), and green = Fantastic Lava (FL; tephra Unit 3). (For interpretation of the references to color in this figure legend, the reader is referred to the web version of this article.)

dominant tephra Units 2 and 3 (Fig. 2; yellow star in Fig. 1). Ten tephra samples were collected from distinctive layers throughout the section. Field descriptions of each sample and a corresponding field photo are labeled in Fig. 2. The lowermost sample from the column is LCC-1-9, and is interpreted to be ~10 cm from the base of Unit 2, the first main explosive phase of the eruption. In the field, early erupted units LCC-1-9, LCC-1-8, LCC-1-7, LCC-1-6 (associated with Heiken's Unit 2), are easily distinguished from the later erupted units (LCC-1-5, LCC-1-4, LCC-1-3, LCC-1-2, and LCC-1-1; associated with Heiken's Unit 3) because they are dominated by relatively large, highly vesicular golden tephra clasts. Early erupted units (LCC-1-9 through LCC-1-6) also have a restricted area (~40 km^2 for the 5-cm isopach) and both the deposit and tephra characteristics suggest the eruption was primarily Strombolian in eruptive style (Marks, 2012). These four lower tephra layers are overlain by a dark fine ash layer (LCC-1-5), interpreted as a transitional unit. The upper tephra units (LCC-1-4 through LCC-1-1) are markedly finer grained, and the lowermost unit (LCC-1-4), in particular, is composed of dense microcrystalline clasts. Together with the larger areal extent (~100 km^2 for the 5-cm isopach) and volume, these characteristics were interpreted by Marks (2012) to indicate a more explosive eruptive style for the later erupted units. The uppermost layer, LCC-1-1, is overlain by a soil with scattered 1915 Lassen Peak pumice lapilli (Fig. 2).

There are several curious aspects of the Cinder Cone deposits and by extension, both the underlying magmatic system and the eruptive sequence. First, there are ubiquitous quartz xenocrysts in all of the basaltic andesite-andesite lava flows and tephra layers (Clynne et al., 2000). Second, the bulk composition of lava changed over time in composition from 53.5 to 59 wt% SiO_2 through the OB and PD flows and subsequently from 55 to 58 wt% SiO_2 through the FL flows (Clynne, 2011). The tephra mimic these changes: early erupted tephra vary compositionally through stratigraphy in a manner similar to the PD flows, and late erupted tephra varies compositionally

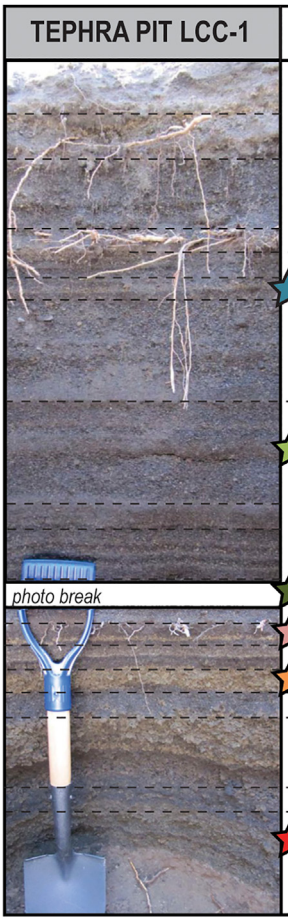

TEPHRA PIT LCC-1	Approx. Thickness	Sample Name	Sample Description
	--	--	Topsoil
	--	--	Lassen 1915 white pumice layer
	10 cm	LCC-1-1	Coarse ash; vaguely laminated; abundant lava chips
	2.5 cm	--	Fine ash layer with abundant roots
	2.5 cm	--	Coarse ash layer
	1 cm	LCC-1-2	Tan fine ash layer
	15 cm	LCC-1-3	Two coarse ash layers separated by a thin fine ash layer
	15 cm	LCC-1-4	Two coarse ash layers separated by a thin fine ash layer
	2.5 cm	--	Fine ash layer
	17.5 cm	--	Alternating cm-size layers of coarse and fine ash
	2.5 cm	LCC-1-5	Fine ash layer that separates FL from PD compositions
	1 cm	LCC-1-6	Tan Lapilli layer
	5 cm	--	Dark coarse ash layer intermingled with tan tephra
	3.75 cm	LCC-1-7	Tan Lapilli layer
	3.75 cm	--	Dark ash with dense clasts
	20 cm	LCC-1-8	Coarse tan lapilli layer, inversely graded
	5 cm	--	Dark coarse ash layer
	12.5 cm	LCC-1-9	Coarse ash layer with mixed tan and black clasts

Fig. 2. Field photo of the cone proximal ~1 m tephra section (LCC-1) from which samples are derived (Location indicated in Fig. 1). The associated table provides unit descriptions and approximate thicknesses of individual tephra units, which are not to scale because of the angle of the photograph. Samples utilized for melt inclusion analyses are labeled and color-coded (star symbols) by tephra unit. Colors will be used throughout the manuscript. (For interpretation of the references to color in this figure legend, the reader is referred to the web version of this article.)

in a manner similar to the FL flows (tephra samples correlative to OB were not acquired). Third is the apparent change in eruptive style that accompanies the reversal in the compositional trend of the magma. Not only does each eruptive phase cycle from initially explosive to primarily effusive, but each cycle becomes more explosive over time. That is, Unit 2 tephra exhibits a primarily Hawaiian to Strombolian eruptive style, whereas Unit 3 is interpreted to have been deposited as the result of a violent Strombolian phase (Marks, 2012). Although a detailed textural analysis is not available for Unit 1 tephra, its low volume and distribution suggest this initial eruptive phase was a short-lived and low-explosivity event.

Of the ten tephra samples collected, six were chosen for MI analysis that best represent the main eruptive phases and thus the chemical transitions throughout the eruptive sequence. Tephra from LCC-9, LCC-7, and LCC-6 represent the early erupted tephra, LCC-5 and LCC-4 are interpreted to represent the transition in eruptive phases (closing phase of Unit 2 and opening phase of Unit 3, respectively), and LCC-2 represents the late erupted tephra (Fig. 2). The results of Marks (2012) suggest Unit 1 was not sampled at this locality.

4. Methods

4.1. Melt inclusion sample preparation

The ash-sized tephra fraction (<2 mm) was used for MI analyses because it quenches more rapidly than lava flows, bombs, and lapilli sized tephra clasts, minimizing the potential effects post-eruption modification (Lloyd et al., 2013). Loose olivine crystals, 1 mm to 250 μm in size, were hand-picked from the washed and sieved tephra (Supplementary Fig. 1). The olivine crystals were treated in HBF_4 to remove adhering glass and examined in immersion oils (refractive index 1.675) to locate MI. Olivine crystals from the deposit are generally euhedral and most contain chrome-spinel inclusions. Nearly all MI also contained a 10 to 30-μm-diameter vapor bubble. Olivine crystals hosting fully enclosed and glassy MI were mounted in crystal bond on glass slides and prepared as doubly polished wafers. Wafers were immersed in acetone to completely dissolve the crystal bond before Fourier transform infrared spectroscopy (FTIR) analysis, and subsequently mounted in epoxy for electron probe micro-analysis (EPMA) and laser ablation inductively coupled plasma mass spectrometry (LA-ICP-MS) analyses.

4.2. Analytical procedures

4.2.1. FTIR

H_2O and CO_2 concentrations were measured at the University of Oregon using a Thermo-Nicolet Nexus 670 FTIR spectrometer interfaced with a Continuum IR microscope. Concentrations were calculated from IR peak absorbance using the Beer–Lambert law: $C = MA/\rho d\varepsilon$, where M is the molecular weight of H_2O or CO_2, A is the measured absorbance of the band of interest (3550 cm^{-1} for H_2O, and 1515 and 1435 cm^{-1} for CO_2), ρ is the glass density at room temperature (calculated with major element compositions deter-

mined by EPMA), d is the thickness of the MI wafer (measured by micrometer and interference fringes), and ε is the molar absorption coefficient. An absorption coefficient of 63 L/mol cm (Dixon et al., 1995) was used for H_2O. The absorption coefficients for CO_2 were calculated for each inclusion based on the major element composition (283–345 L/mol cm; Dixon and Pan, 1995). This method relates the absorption coefficient to the molar Na/(Na + Ca) of the glass and is calibrated for the range of compositions for our samples. Peak height measurements and background subtraction for the carbonate peaks at 1515 and 1435 cm^{-1} were calculated using a peak fitting program (S. Newman, unpublished). This method yields values for experimental glasses (Dixon et al., 1995) that are comparable to the reference-glass subtraction and hand drawn background method upon which the CO_2 solubility relations and molar absorption coefficient calibration were established (J. Dixon, pers. commun.). Raw and corrected MI H_2O and CO_2 compositions can be found in Supplementary Table ST1 and ST2.

4.2.2. EPMA

Melt Inclusions and host olivine were analyzed for major elements, S, and Cl on the Cameca SX-100 electron microprobe at the University of Oregon CAMCOR MicroAnalytical Facility. MI glass compositions and host olivine were analyzed with a 10 nA or 50 nA, 10-μm diameter beam and 15 kV accelerating voltage for major elements. Time dependent intensity corrections were made for Na, K, Si, and Al, and these elements were analyzed first at 10 nA. Subsequently, the beam current was increased to 50 nA for analysis of Mg, Fe, Ca, Ti, P, S, and Cl. Individual inclusion analyses are averages of three point analyses. Olivine compositions are also averages of three point analyses taken ~100 μm from inclusion and crystal edges to ensure analysis of olivine unaffected by later stage diffusion. Raw and corrected MI compositions can be found in Supplementary Table ST1 and ST2, respectively.

4.2.3. LA-ICP-MS

Melt inclusions and host olivine were subsequently analyzed for a suite of trace elements on the Photon Machines Analyte G2 193 nm ArF "fast"Excimer Laser system at Oregon State University, using 50 μm spot size with a 5 Hz pulse rate. Measured trace element concentrations were determined by reference to GSE-1G glass as a calibration standard and using 43Ca as an internal standard (see Loewen and Kent, 2012, for details). BHVO-2G, BCR-2G, and GSD-1G glasses were also analyzed to monitor accuracy and precision, and the analyzed values were within 10% of accepted values.

A larger set of olivine phenocrysts from LCC-2, LCC-4, and LCC-9 were also analyzed at Lamont-Doherty Earth Observatory. Data were acquired using a NewWave 193 nm ArF Excimer laser with a PQExcell ICPMS operated in continuous line scan mode using a circular laser spot (25 μm for data acquisition and 50 μm for pre-ablation) from the core to the rim of each olivine crystal. Scan speed was 3 μm/s (30 μm/s during pre-ablation) and laser pulse rate was held at 15 Hz. Calibration curves were obtained using a set of reference glasses (BIR, BHVO, GOR132-G and GOR128-G) for 15 elements (Li-7, Mg-26, Al-27, P-31, Ca-44, Sc-45, Ti-47, V-51, Cr-52, Mn-55, Fe-57, Co-59, Ni-60, Cu-65, Zn-66; see Ruprecht and Plank, 2013, for details). Recent analyses with the used analytical procedure have shown that Ca-44 can occasionally be affected by the isobaric interference of Si-28-O-16, thus limiting the use of Ca-44 here. MPI-Ding Gorgona glasses were specifically included to obtain good calibrations for elements compatible in olivine (most notably Ni). Mg-26 was used as internal standard and calculated via stoichiometry (assuming an ideal solid solution of $(Mg,Fe)_2SiO_4$) from count rates of Mg-26 and Fe-57. New calibration curves were obtained prior to each sample. Reference glasses KL2-G and ML3B-G, and San Carlos olivine (USNM 111312/42) mounted in indium, were also analyzed to monitor accuracy and precision. Olivine and MI trace element compositions can be found in Supplementary Table ST3 and ST1, respectively.

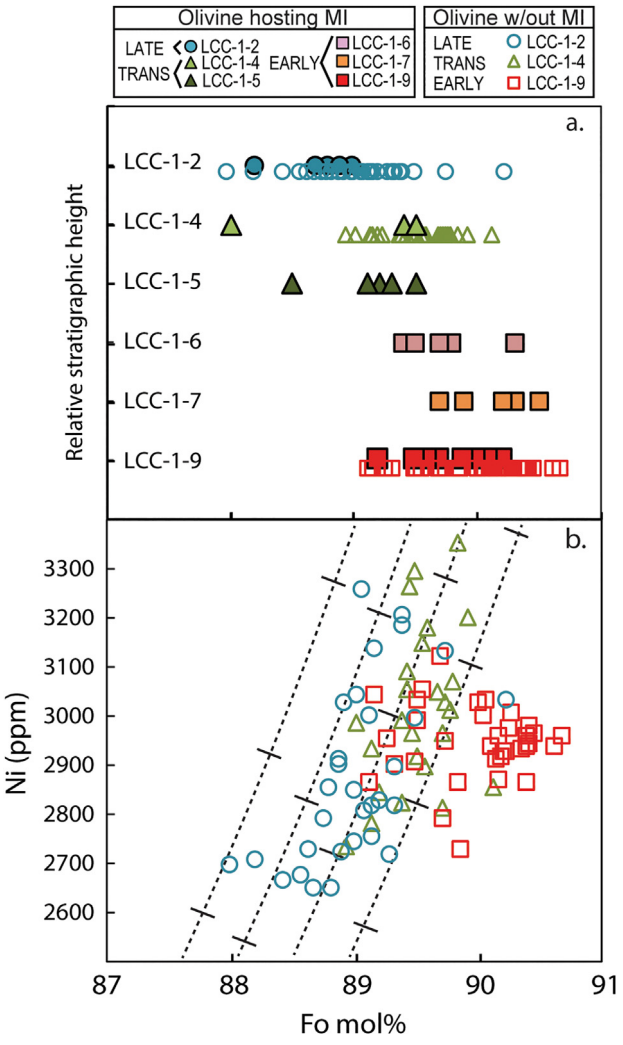

Fig. 3. Olivine phenocryst compositions. a) Forsterite content of olivine hosting melt inclusions (filled symbols) and additional olivine phenocrysts measured by LA-ICP-MS (without melt inclusions; open symbols) ordered by relative stratigraphic height. See Fig. 2 for a more detailed stratigraphy. b) Ni versus Fo for olivine phenocryst cores (not hosting analyzed melt inclusions) measured by LA-ICP-MS. Panels a) and b) exclude data from olivine xenocrysts, as described in Section 5.1. Solid black lines represent olivine fractionation curves, labeled with tick marks which each represent 1% of olivine fractionation.

5. Results

5.1. Olivine compositions

The host olivine have core compositions of $Fo_{88.0–90.5}$. The larger populations of analyzed olivine phenocrysts from LCC-1-9, LCC-1-4, and LCC-1-2 overlap with the MI host olivine compositions (Fig. 3a), and typically exhibit broad, homogenous cores and thin (10-30 μm) Fe-rich rims. From this larger population, 10 crystals were identified as xenocrysts because they have variable zoning patterns and contain cores of $Fo_{78–87}$. These xenocrysts are excluded from Fig. 3 because they are not representative of the main phenocryst populations. The olivine hosts for analyzed MI have high-Fo core compositions, with early erupted tephra clasts displaying more Mg-rich olivine cores ($Fo_{89–90.5}$) than later erupted tephra ($Fo_{88–89}$) (Fig. 3). Early and late erupted olivine phenocrysts also have distinc-

tive trace element compositions (Fig. 3b), with the high-Fo cores of early erupted olivine showing a more restricted range in Ni.

5.2. Post-entrapment crystallization and Fe-loss corrections

The MI analyzed in this study were all sampled from rapidly quenched tephra. However, MI are commonly affected by crystallization of olivine along the walls of the inclusion and by Fe diffusive loss during the time between trapping and eruption. If the measured composition of a MI is not in equilibrium with the surrounding host olivine, then the MI has likely experienced post-entrapment crystallization (PEC; Danyushevsky et al., 2000). The original MI composition can be estimated by incrementally adding equilibrium olivine back into the melt until it is in equilibrium with its host olivine. In this study, Petrolog 3.1 (Danyushevsky and Plechov, 2011) was used to determine original MI compositions and to calculate the percent of olivine crystallized from the MI after entrapment. For this correction, we used Fe-Mg partition coefficients (K_d) between the melt and host olivine from Danyushevsky (2001). Oxygen fugacity was determined using the partitioning of V between the MI and host olivine using methods of Mallmann and O'Neill (2009). The oxygen fugacities of the most primitive MIs were ΔQFM +1.4 (±0.4), with no distinct difference between eruptive units.

Post-entrapment crystallization corrections also require an estimate of the initial Fe content of the MI prior to Fe-loss by diffusion. Bulk tephra analyses from Cinder Cone were used as a proxy to estimate the original Fe contents. Primitive lavas in the Lassen region have 7–8 wt% FeO^T which overlaps with or is slightly higher than the values for Cinder Cone lavas and bulk tephra (5.5–7 wt% FeO^T). Based on this comparison we assumed that Cinder Cone melts initially had 7 wt% FeO^T. Melt inclusion compositions required 5–15.6% olivine addition to reach equilibrium with their host olivine, a range typical for olivine-hosted melt inclusions (e.g., Johnson et al., 2009; Ruscitto et al., 2010). Volatile and incompatible trace element concentrations in the MI were also corrected for PEC using the Petrolog 3.1 results.

5.3. Major element compositions

We present data for 43 MI, 23 of which are from early units, 12 from transitional units, and 8 from the late erupted tephra (Table 1; Supplementary Table TS1). Corrected MI are basaltic to basaltic andesite in composition (Fig. 4), and most fall in a narrow range of SiO_2 contents (~51–53 wt% on a volatile-free basis). Variability in total alkalis, however, shows compositional differences in MIs from different units. Early erupted units (LCC-9, LCC-7, LCC-6) have lower alkalis (~3.5–4 wt% $Na_2O + K_2O$) compared to middle and late erupted units (LCC-5, LCC-4, LCC-2), which have higher values (~4–4.5 wt%). Middle erupted or transitional units (LCC-4 and LCC-5) display the most compositional variability and contain the greatest number of inclusions that have high concentrations of both SiO_2 and alkalis. This pattern is also apparent in the concentrations of other major elements, such as MgO and CaO, which are elevated in early erupted MIs compared to late erupted MIs, but highly variable in the transitional units (Fig. 5). Because early and late erupted MIs are easily identified by most major elements and are found within tephra units that display distinct deposit characteristics (Marks, 2012), for simplicity, we will refer to the average early erupted MI composition as the early magma batch and the average late erupted MI composition as the late magma batch.

Interestingly, the differences in alkalis between early erupted and late erupted MIs are mirrored in the total alkali concentrations of lava and bulk tephra (Fig. 4). While most MIs have distinctly lower SiO_2 than the lavas and bulk tephra (Fig. 4), melt inclusions

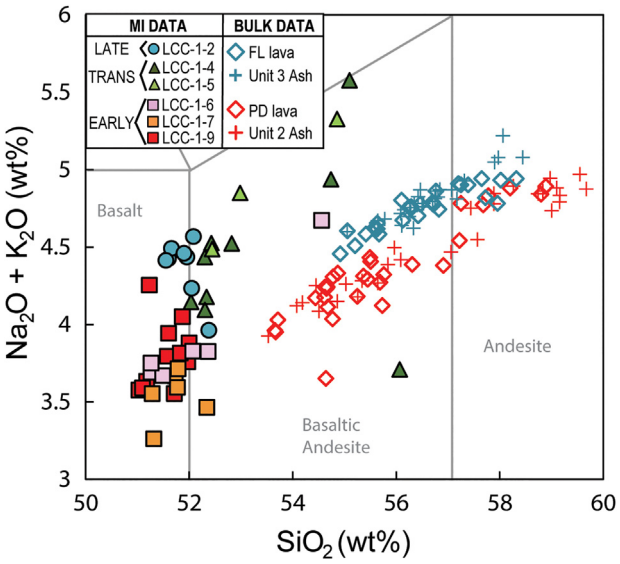

Fig. 4. Melt inclusion total alkalis and SiO_2 compared to bulk tephra and lava. Filled symbols are melt inclusions from this study corrected for PEC and normalized on a volatile-free basis. Bulk lava (open diamonds) and tephra (crosses) are from Clynne (2011). Classification boundaries for basalt, basaltic andesite, andesite, trachy-andesite, and trachy-basalt from Le Bas et al. (1986). Uncertainty is less than the symbol size (Supplementary Table ST1).

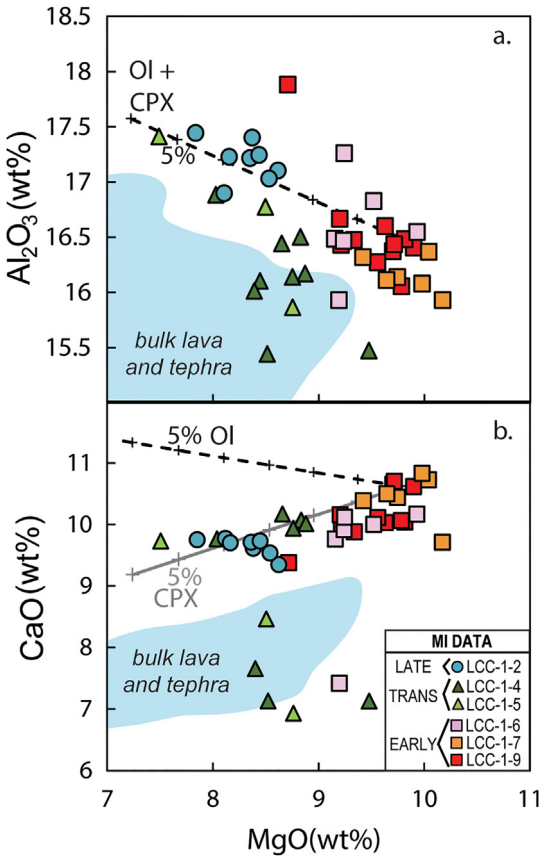

Fig. 5. Melt inclusion MgO vs. Al_2O_3 and CaO. MgO vs. a) Al_2O_3 and b) CaO for MI compositions (corrected for PEC; normalized on a volatile-free basis) compared with lava and bulk tephra (shaded blue region; Clynne, 2011). Fractionation curves calculated using Petrolog 3.1 for olivine (Ol, black dashed line; Danyushevsky and Plechov, 2011) and Rhyolite-MELTS at 10 kbar for clinopyroxene (CPX, grey line; Gualda et al., 2012), with tick marks representing 1% fractionation. Uncertainty is less than symbol size (see Supplementary Table ST1). (For interpretation of the references to color in this figure legend, the reader is referred to the web version of this article.)

Table 1
Corrected melt inclusion compositions.
Each row represents the composition of an individual melt inclusions corrected for post-entrapment crystallization, as described in Section 4. Methods.
Samples are named LCC-1-*X*-*Y*-*Z* where LCC-1 refers to the tephra pit (as described in Fig. 2) *X* refers to the sampled tephra units (Fig. 2), Y refers to the individual olivine phenocrysts and *Y* refers to an individual melt inclusion (e.g., an individual olivine phenocryst may host 2 melt inclusions).
*Reported CO_{2max} values represent the composition corrected for CO_2-loss to vapor bubbles. [V] Indicates melt inclusions that do not have vapor bubbles, and thus were not corrected for CO_2-loss to vapor bubbles.
Fo_host values refer to the forsterite content of the olivine hosting the analyzed melt inclusion.

Sample	SiO_2	TiO_2	Al_2O_3	MgO	CaO	Na_2O	K_2O	H_2O	*$CO_{2\,(ppm)}$	FO_Host	Pb	Li	Sc	Th	La	Sr/Nd	Zr/Nb
LCC-1-9-01	50.64	0.84	16.06	8.93	9.74	3.13	0.83	2.48	1946	89.70	–	–	–	–	–	–	–
LCC-1-9-02	49.76	0.91	17.37	8.42	9.10	3.32	0.81	2.94	994	89.20	–	–	–	–	–	–	–
LCC-1-9-06	49.47	0.83	15.94	9.47	10.27	2.78	0.69	3.19	2913	90.20	2.40	5.84	30	1.29	8.38	31.70	18.14
LCC-1-9-07	50.23	0.80	16.03	9.41	9.76	2.67	0.79	2.97	1252	90.00	2.91	9.69	31	1.65	7.83	35.83	17.46
LCC-1-09-09	50.28	0.77	15.88	9.51	9.37	2.74	0.79	2.72	1781	90.10	2.87	15.76	31	1.66	8.08	24.43	22.16
LCC-1-9-04-1	50.17	0.82	16.23	8.86	9.85	3.06	0.78	2.89	1162	89.60	2.90	7.24	27	1.66	7.59	30.53	17.78
LCC-1-9-04-2	50.41	0.80	16.00	8.94	9.55	2.92	0.85	3.18	1453	89.60	2.80	7.60	27	1.53	7.03	32.37	17.35
LCC-1-9-10	50.29	0.78	16.21	9.29	9.75	2.92	0.79	2.63	2631	90.00	–	–	–	–	–	–	–
LCC-1-9-16-1	49.53	0.80	15.88	9.26	10.30	2.87	0.66	3.35	2696	90.00	1.66	4.84	29	1.12	6.57	34.84	16.27
LCC-1-9-16-2	49.43	0.81	15.93	9.28	10.34	2.82	0.66	3.38	2766	90.00	2.13	7.55	29	0.99	6.44	34.30	15.46
LCC-1-9-18	50.40	0.80	15.85	9.20	9.81	2.96	0.76	2.88	2514	89.90	–	–	–	–	–	–	–
LCC-1-7-02	50.23	0.76	16.05	9.73	10.47	2.59	0.60	2.25	2574	90.30	–	–	–	–	–	–	–
LCC-1-7-03	50.78	0.76	15.86	9.50	10.22	2.95	0.65	1.95	2194	90.20	–	–	–	–	–	–	–
[V]LCC-1-7-04	50.48	0.78	15.84	9.77	10.63	2.89	0.61	1.68	892	90.50	–	–	–	–	–	–	–
LCC-1-7-05	50.75	0.77	15.49	9.70	9.41	2.60	0.77	3.19	1325	90.20	3.95	17.02	29	1.27	7.39	35.32	17.52
LCC-1-7-08	50.24	0.77	15.86	9.03	10.06	2.92	0.69	3.10	1782	89.70	2.82	7.11	29	1.18	7.07	36.65	16.95
LCC-1-7-10	50.27	0.78	15.68	9.25	10.18	2.84	0.66	3.02	2196	89.90	2.42	7.32	26	1.01	6.34	36.50	15.21
LCC-1-6-01	49.92	0.82	16.14	9.57	9.87	2.90	0.70	2.74	2598	90.30	2.88	9.04	25	1.08	7.05	34.24	13.48
LCC-1-6-02	51.00	0.81	16.08	8.83	9.48	2.95	0.78	2.73	1540	89.40	3.02	7.04	25	1.58	7.86	36.79	15.57
LCC-1-6-06	50.05	0.85	16.38	9.16	9.70	2.82	0.75	2.91	2022	89.80	2.80	9.05	26	1.44	7.32	34.06	15.23
LCC-1-6-07	50.57	0.84	16.02	8.87	9.61	2.94	0.78	3.00	2735	89.50	–	–	–	–	–	–	–
LCC-1-6-08	50.29	0.82	16.94	9.02	9.89	2.91	0.77	2.02	1392	89.70	–	–	–	–	–	–	–
[V]LCC-1-6-10	53.65	0.70	15.67	9.02	7.24	3.15	1.45	1.76	1122	89.70	8.29	35.27	21	3.26	9.51	28.38	14.58
LCC-1-5-01–1	50.83	0.81	16.13	8.56	9.81	3.20	0.85	2.43	2347	89.30	–	–	–	–	–	–	–
LCC-1-5-01–2	50.94	0.81	15.76	8.56	9.72	3.25	0.82	2.78	2419	89.30	–	–	–	–	–	–	–
[V]LCC-1-5-03	52.20	0.87	15.90	8.38	9.60	3.55	0.91	1.24	738	89.20	3.14	9.17	26	1.60	8.41	35.35	16.01
LCC-1-5-04	54.25	0.77	15.86	8.37	7.52	3.43	1.46	0.96	897	89.10	9.74	33.23	19	2.69	10.56	28.70	14.65
LCC-1-5-05	51.45	0.89	15.87	8.61	9.73	3.54	0.82	1.72	2525	89.50	–	–	–	–	–	–	–
LCC-1-5-07	51.84	0.85	16.29	8.60	10.04	3.21	0.85	0.99	2827	89.30	–	–	–	–	–	–	–
[V]LCC-1-5-11-1	53.89	0.67	15.11	8.30	6.92	3.69	1.77	2.29	1305	89.30	9.82	51.64	18	2.84	9.30	29.04	14.59
[V]LCC-1-5-11-3	55.30	0.67	15.28	9.28	6.97	1.94	1.72	1.49	0	89.30	–	–	–	–	–	–	–
LCC-1-5-12	51.46	0.78	16.57	7.87	9.56	3.41	1.03	1.93	1883	88.50	3.81	11.13	21	1.46	8.75	36.31	15.04
LCC-1-4-05	52.66	0.93	16.64	8.56	8.33	3.25	1.56	0.68	1637	89.40	2.62	6.24	20	1.24	6.47	35.31	13.85
LCC-1-4-06	52.08	0.94	17.25	7.57	9.60	3.45	1.00	0.71	0	88.00	14.00	68.95	28	4.78	14.92	29.67	13.37
[V]LCC-1-4-13	50.73	0.92	16.28	8.65	9.54	3.38	0.84	1.97	1240	89.50	–	–	–	–	–	–	–
LCC-1-2-01	50.98	0.96	16.54	7.94	9.53	3.58	0.89	2.19	1402	88.70	3.91	10.53	26	1.70	9.13	32.56	12.15
LCC-1-2-02	50.96	0.94	16.66	8.32	9.07	2.91	0.95	2.82	1692	88.80	–	–	–	–	–	–	–
LCC-1-2-04	50.60	0.95	16.57	8.24	9.24	3.22	0.90	2.89	2645	88.90	2.95	7.71	24	1.43	8.99	32.40	14.14
LCC-1-2-05	50.55	0.97	17.04	8.20	9.39	3.42	0.92	2.11	1950	89.00	–	–	–	–	–	–	–
LCC-1-2-07	50.57	0.95	16.85	8.18	9.47	3.49	0.91	2.20	1843	89.00	2.97	9.59	27	1.61	9.36	31.26	12.97
LCC-1-2-08	50.76	0.94	17.03	7.66	9.50	3.43	0.91	2.38	1725	88.20	3.48	8.50	28	1.72	9.53	32.29	13.73
LCC-1-2-09	50.83	0.94	16.87	7.98	9.47	3.46	0.91	2.14	1392	88.70	–	–	–	–	–	–	–
LCC-1-2-10	49.99	0.92	16.74	8.12	9.41	3.40	0.89	3.14	2007	88.90	–	–	–	–	–	–	–

with elevated SiO_2 (>54 wt%), mostly from the transitional units, overlap with bulk lava and tephra in MgO and Al_2O_3 contents.

5.4. Volatile concentrations

H_2O and CO_2 concentrations measured (uncorrected) at Cinder Cone range from 0.74 to 3.7 wt% and 0–1545 ppm, respectively (Fig. 6), similar to values for other nearby scoria cones (Walowski et al., 2015, 2016) and cones in the central Oregon Cascades (Ruscitto et al., 2010; Ruscitto et al., 2011; Le Voyer et al., 2010). However, a number of recent studies have shown that MIs commonly experience post-entrapment changes that decrease their dissolved H_2O and CO_2 concentrations (Esposito et al., 2011; Gaetani et al., 2012; Bucholz et al., 2013; Lloyd et al., 2013; Hartley et al., 2014; Moore et al., 2014; Wallace et al., 2015). The measured dissolved concentrations therefore represent a minimum estimate of the initial H_2O and CO_2 contents of the magma during entrapment.

Most basaltic MIs, including nearly all MIs in this study, contain a vapor bubble, the size of which can be used to determine if it is primary (co-entrapped with melt) or formed after entrapment (Riker, 2005). Shrinkage bubbles form after entrapment as a result of the pressure drop caused by crystallization along the host-inclusion interface and thermal contraction of the melt (Roedder, 1979; Lowenstern, 1995). Because CO_2 has a much lower solubility than H_2O, it strongly partitions into the bubble, leaving only a fraction of the CO_2 dissolved in the melt compared to that at the time of entrapment (Esposito et al., 2011; Hartley et al., 2014; Moore et al., 2014). Recent work suggests that 40–90% of the total CO_2 in the MI can be lost to this shrinkage bubble (Moore et al., 2014; Wallace et al., 2015; Aster et al., 2016), leading to a drastic underestimation of entrapment depths when only dissolved CO_2 is taken into account. To correct for CO_2 loss, we used a modified calculation based on the methodology of Riker (2005), Wallace et al. (2015), and Aster et al. (2016). Comparisons of this method with results of experimental redissolution of CO_2 in shrinkage bubbles (Wallace et al., 2015; Tuohy et al., 2016) and Raman spectroscopic determination of CO_2 densities in bubbles (Aster et al., 2016) show reasonable agreement. First, we estimate the size of the vapor bubble at the time of eruption. This bubble volume (V_{bub}) is formed as the result of cooling-induced crystallization (PEC) and melt contraction as a function of the change in temperature between entrapment and

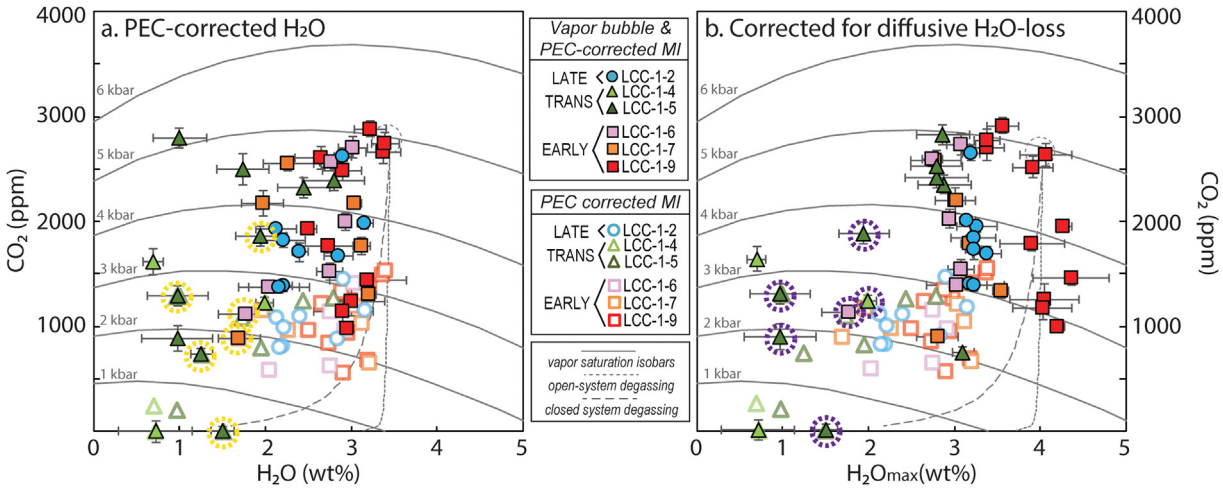

Fig. 6. Melt inclusion corrected H_2O (wt%) vs. CO_2 (ppm). Open colored symbols in Panels a) and b) are PEC-corrected-only values. Filled colored symbols in Panel a) represent PEC-corrected H_2O (wt%) values with CO_2 (ppm) corrected for loss to vapor bubbles. Filled colored symbols in Panel b) represent melt inclusions corrected with H_2O (wt%) values corrected for hydrogen diffusive loss and CO_2 (ppm) corrected for loss to vapor bubbles. Solid grey bars are vapor saturation isobars calculated using rhyolite-MELTS (Ghiorso and Gualda, 2015). Open and closed system degassing paths (dashed lines), were calculated using VolatileCalc (Newman and Lowenstern, 2002) and the composition of melt inclusion LCC-1-9-16-1. Melt inclusions that do not have a vapor bubble were not corrected for CO_2-loss, and are highlighted by yellow dashed circles in panel a). Melt inclusions that had $K_2O > 1$ wt% indicative of crustal contamination were not corrected for H_2O-loss and are highlighted by purple dashed circles in panel b). Corrections are described in the main text, and data can be found in Supplementary Tables ST1, ST2, and ST4. Error bars are one standard deviation. (For interpretation of the references to colour in this figure legend, the reader is referred to the web version of this article.)

pre-eruption (ΔT). We use the phase equilibria of the most primitive MI compositions calculated with rhyolite-MELTS (which is also optimized for basaltic compositions at the pressures of interest; Ghiorso and Gualda, 2015) and the volume and thermal expansion data for silicate melts (Lange and Carmichael, 1990) and olivine (Kumazawa and Anderson, 1969; Suzuki, 1975) to derive an equation for the Cinder Cone magmas:

$$V_{bub}\ (\%) = 0.0092\ \Delta T \quad (1)$$

For each individual MI, we used Petrolog 3.1 to estimate the ΔT and then Eq. (1) to estimate V_{bub}. Melt inclusions that did not contain a vapor bubble were excluded from this correction. Although the absolute temperatures calculated with rhyolite-MELTS (Ghiorso and Gualda, 2015) and Petrolog 3.1 (Danyushevsky and Plechov, 2011) are different, the ΔT calculated for each MI from the two methods is similar (Aster et al., 2016).

We used this estimate of the pre-eruption V_{bub}, the pre-eruption temperature, and the dissolved H_2O and CO_2 concentrations of each inclusion to determine the mol% CO_2 in the equilibrium vapor phase using rhyolite-MELTS (Ghiorso and Gualda, 2015). We then used the Redlich-Kwong equation of state to determine the molar volume of CO_2 in the vapor bubble. This allows us to estimate the mass of CO_2 in the bubble and then add it to the mass of CO_2 dissolved in the quenched glass to get an estimate of the total dissolved CO_2 concentration in the MI at the time of trapping. The results of the CO_2 restoration calculations suggest that 5–84% (avg. 52%) of the initial dissolved CO_2 in the MIs at the time of trapping was lost to vapor bubbles during post-entrapment crystallization. Corrected concentrations of CO_2 are shown in Fig. 6 and in Table 1, and a table detailing the correction method for each inclusion can be found in Supplementary Table ST4.

The H_2O contents of MIs can also be modified after entrapment. Experimental studies have shown that at magmatic temperatures, olivine-hosted MIs can lose nearly all of their H_2O in hours to days via H^+ (proton) diffusion, depending on temperature and H_2O content of the surrounding melt (Gaetani et al., 2012; Bucholz et al., 2013). To investigate whether MIs from Cinder Cone have lost H by diffusion, we compared S/K_2O and H_2O/K_2O ratios: correlated low values would indicate that lower MI H_2O contents record early degassing of the melt (e.g., Johnson et al., 2010). The observed variations in H_2O/K_2O and more restricted range of S/K_2O, however, suggest that the H_2O variations may be the result of variable diffusive loss. To correct for post-entrapment H loss by diffusion, following Lloyd et al. (2013), we assumed that all MI initially had H_2O/K_2O values similar to that of the highest measured value for each unit. This correction procedure should yield the maximum likely initial H_2O content for each inclusion (Fig. 6b; Table 1). Melt inclusions with >1 wt% K_2O were not corrected for H-loss by diffusion because they likely experienced crustal contamination and may have been trapped after some degassing of H_2O. The maximum estimated H_2O values (Fig. 6b) can be compared with H_2O values that have only been corrected for post-entrapment crystallization (Fig. 6a), as these provide upper and lower bounds, respectively, for the H_2O contents at time of trapping.

Trapping pressures for the restored H_2O and CO_2 concentrations were calculated using solubility relations of Ghiorso and Gualda (2015), which is the most up-to-date model with the largest calibration dataset. The solubility model results are similar to those from Iacono-Marziano et al. (2012) at the relevant H_2O and CO_2 concentrations. The estimated trapping pressures range from ~2.4–4.8 kbar for the vapor bubble and H-loss corrected MIs (Fig. 6). These estimates are 1–2 kbar higher than those estimated from PEC-corrected-only dissolved H_2O and CO_2 contents. Assuming an average crustal density of 2.6 g/cm^2, the determined pressures correlate to entrapment depths of ~9.5–20 km below the surface. Corrected MI fall more closely along open- or closed-system degassing paths (Fig. 6), indicating that they may have been trapped over a range of pressures from vapor-saturated melts, although this may be an artifact of our assumption of initially constant H_2O/K_2O (cf., Lloyd et al., 2013). The high-K_2O MI that were not corrected for H-loss and those that did not contain vapor bubbles were likely trapped at lower pressures (<2 kbar).

5.5. Trace element concentrations

Melt inclusions at Cinder Cone have typical calc-alkaline, subduction-related trace element patterns that show enrichments in large ion lithophile (LILE) and light rare earth (LREE) elements relative to high field strength elements (HFSE) like Nb and Ta (Fig. 7).

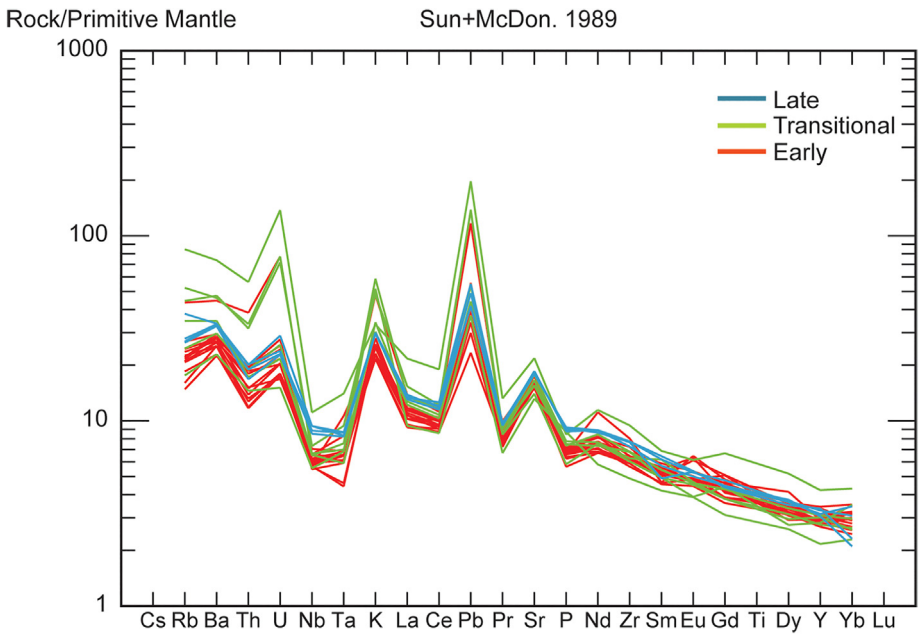

Fig. 7. Spider diagram showing the average melt inclusion composition from each tephra unit. MI trace element compositions corrected for PEC and normalized to Primitive Mantle (PM; Sun and McDonough, 1989). Individual lines represent the trace element compositions of an individual melt inclusion from transitional units (green lines; LCC-1-5 and LCC-1-4), early erupted units (red; LCC-1-6, LCC-1-7, and LCC-1-9), late erupted units (blue; LCC-2). Note that transitional units have more melt inclusion with elevated incompatible trace element concentrations normalized to PM. (For interpretation of the references to color in this figure legend, the reader is referred to the web version of this article.)

MIs from late erupted units have higher concentrations of highly incompatible elements than early erupted MIs. MIs from transitional units with elevated SiO_2 and alkalis are even more enriched in highly incompatible elements such as Sr, Ba, U, and Pb.

6. Discussion

6.1. Crustal contamination

Most MIs have distinctly lower SiO_2 than the lavas and bulk tephra (Fig. 4), which suggests that the Cinder Cone magmas were contaminated by evolved crustal material after most olivine growth and MI entrapment. Furthermore, most olivine crystals ($Fo_{88.5–90.5}$) are not in Fe-Mg equilibrium with the lava and bulk tephra. While we did not analyze matrix glass because of the moderate to extensive groundmass crystallinity, the predicted composition of olivine in equilibrium with the bulk tephra (which is olivine enriched compared to the matrix, but also has varying amounts of quartz xenocrysts) is $Fo_{87–87.5}$. The olivine phenocryst rims are also commonly $Fo_{87–88}$. Therefore, significant chemical evolution of the magma occurred after olivine growth and MI entrapment. The ubiquitous presence of quartz xenocrysts in the tephra and lava suggests that this evolution was caused primarily by crustal contamination. In addition, rare partially melted and/or vesiculated granitic clasts in the lavas likely represent the source of both the abundant quartz and rare K-feldspar xenocrysts.

We calculate the extent of mixing between the low-SiO_2 MI compositions and high-SiO_2 compositions of the granitic xenoliths (Fig. 8). Bulk tephra and lava compositions fall along mixing lines between magma batch 1 (early erupted MI) or magma batch 2 (late erupted MI) and the average granitic xenolith composition. Early erupted PD lava and (Unit 2) tephra can be produced by 10–35 wt% assimilation of granitic basement by magma batch 1 (Fig. 8). Late erupted FL lava and (Unit 3) tephra can be produced by 15–30% assimilation of granitic basement by magma batch 2 (Fig. 8). Rare mafic enclaves in the late-stage FL lava flows are similar in composition to the LCC-1-2 MIs, providing further evidence that the MI represent the parental magma compositions.

Melt inclusions from transitional sample LCC-1-5 have TiO_2 values that fall along mixing lines with the early erupted units. The MI from LCC-1-4, conversely, have TiO_2 contents that fall along mixing lines with the late erupted tephra. These associations are consistent with our interpretations of the tephra stratigraphy, which suggest that LCC-1-5 represents the transitional, waning explosive phase of Unit 2, which is followed by the effusive phase that produced PD2 lava. Subsequently, LCC-1-4 represents the first-erupted material from the explosive phase that produced Unit 3 (Fig. 2). LCC-1-5 also has the largest number of MIs that have contaminated compositions, and which are similar to the lava flows and bulk tephra. This correlation suggests that change in eruptive style from explosive to effusive accompanied increased magma residence time at shallow level to allow time for the observed assimilation and shallow crystallization. This scenario is similar to that suggested for the compositional variation at Parícutin (e.g., Erlund et al., 2010), although it must have occurred over a shorter time scale (<5 years as opposed to 10 years). Evidence for temporary shallow magma storage is also provided by the high groundmass crystallinity of tephra from the transitional samples (particularly LCC-1-4; Marks, 2012).

Further evidence for assimilation of granitic basement is provided by the trace element compositions of MI. Fig. 8 shows that the elevated SiO_2 values of MIs in the transitional units are accompanied by high concentrations of incompatible trace elements, such as Li, Pb, Ba, U. These incompatible trace elements are also found in high concentrations in typical Sierran granites (e.g., Cecil et al., 2012), which are the hypothesized basement rocks in the region and the likely source of the xenoliths. The Li concentrations of the MI appear to be particularly sensitive to the granitic contaminant, as shown by an observed linear correlation of Li with Pb (Supplementary Fig. 3) that clearly separates MIs that have experienced contamination from those that did not.

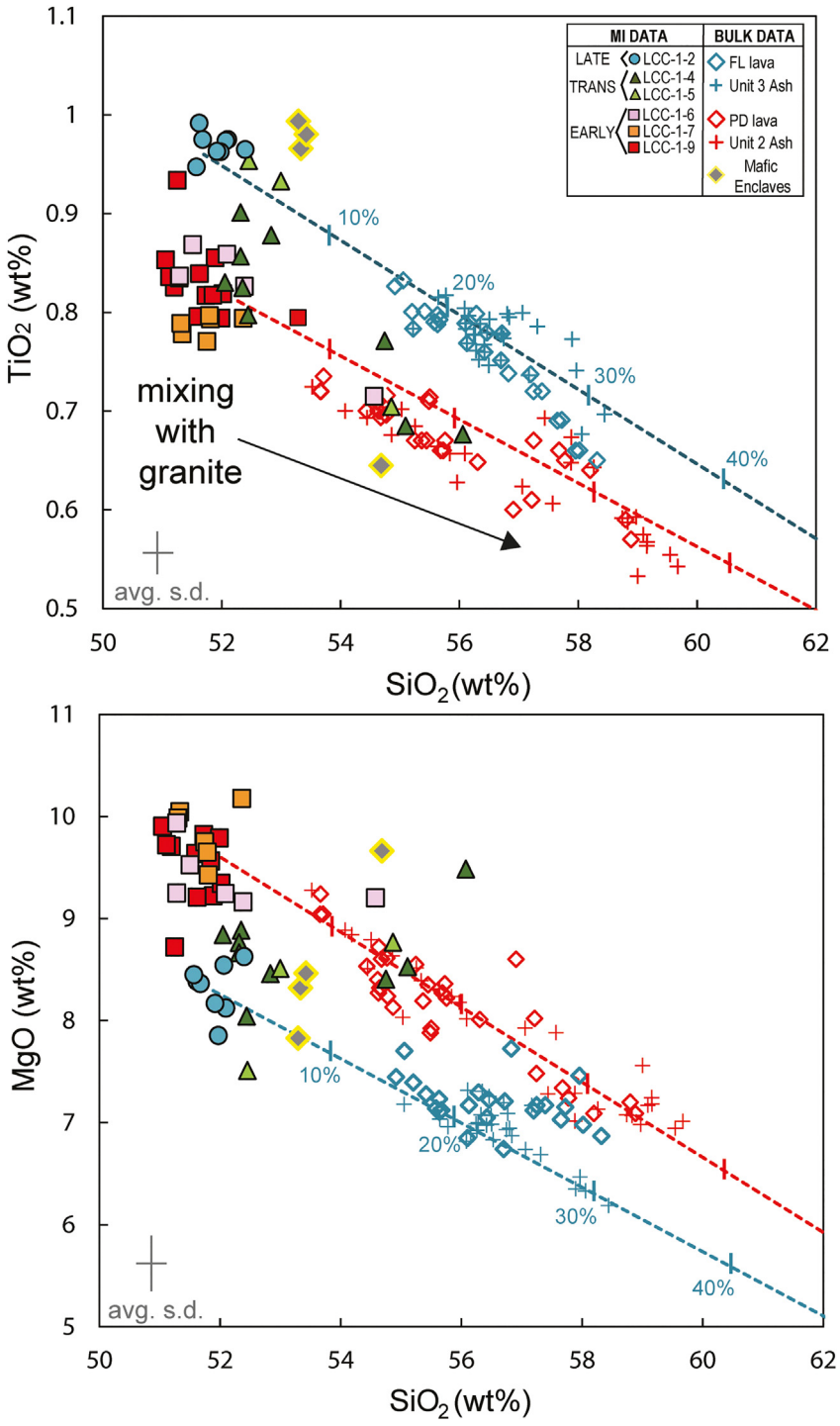

Fig. 8. The SiO_2 vs. a) TiO_2 and b) MgO compositions of MI (corrected for PEC; normalized on a volatile-free basis; filled symbols) lava, bulk tephra, and quenched mafic enclaves (M. Clynne, unpublished data). Curves represent bulk mixing between granitic xenolith compositions (M. Clynne, unpublished data) and average composition of batch 1 (early erupted MI; red dashed curve) and batch 2 (late erupted tephra; blue dashed curve) parental magmas, see text for details. Tick marks represent increments of 10% bulk addition of granitic material. Average analytical uncertainty in upper right hand corner of each panel (see Supplementary Table ST1). (For interpretation of the references to color in this figure legend, the reader is referred to the web version of this article.)

6.2. Parental melt compositions

The olivine phenocrysts in the Cinder Cone tephra have compositions of $Fo_{88.0–90.5}$ and the host crystals for the MI range up to $Fo_{90.2}$. The upper end of the range of olivine compositions overlaps with olivine that would be in equilibrium with mantle peridotite, suggesting the magmas either experienced little to no fractionation prior to MI entrapment, or that there is a relatively refractory mantle source beneath the Lassen region, with olivine >Fo_{90}.

MIs from late erupted LCC-2 show distinct compositional differences relative to early erupted MI (Figs. 5 and 7); they are also hosted in slightly less-magnesian olivine (Fo_{88}; Fig. 3), indicating that they could be related to the early erupted magmas via crystal fractionation. We used Petrolog 3.1 and pMELTS (Ghiorso et al., 2002) to model equilibrium crystallization of the early erupted

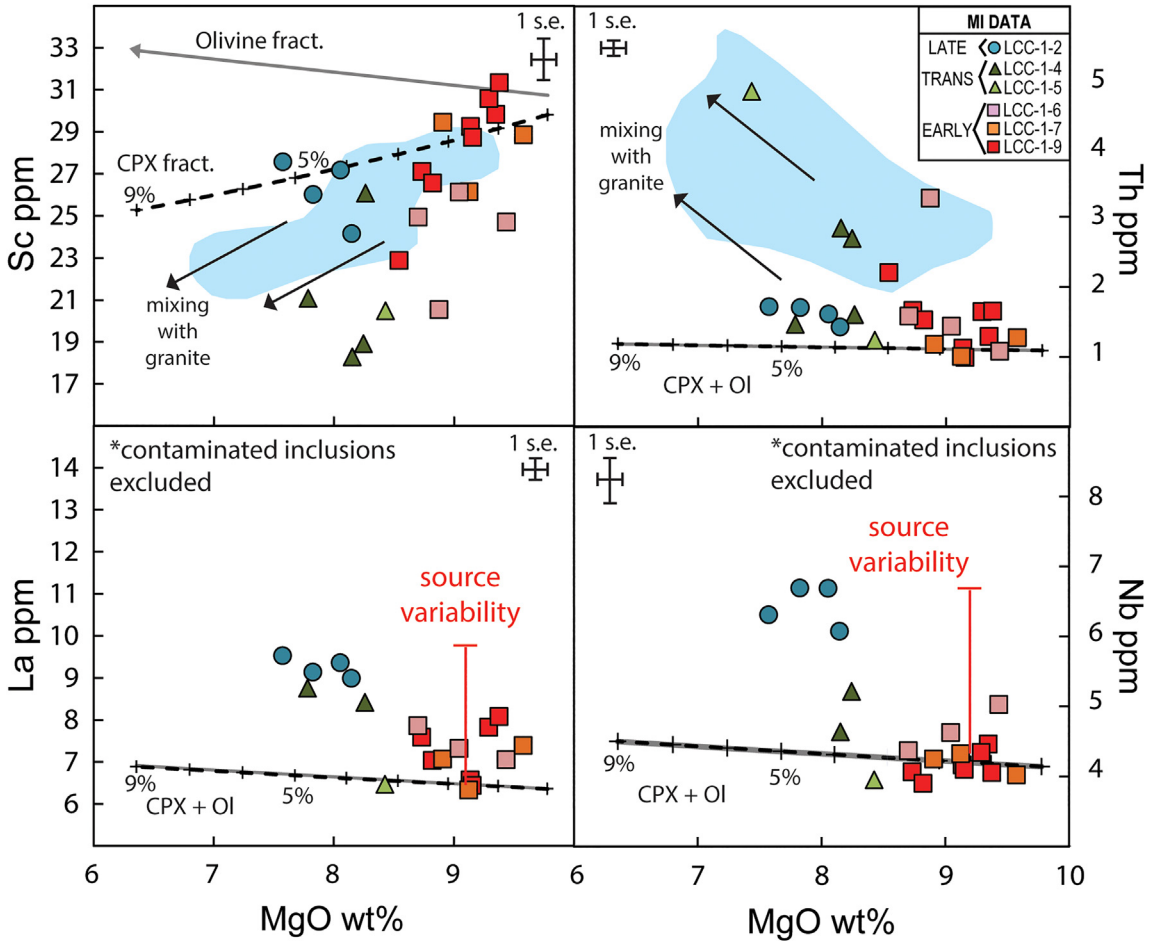

Fig. 9. Melt inclusion MgO vs. trace elements. MgO (normalized on a volatile-free basis) vs. a) Sc, b) Th c) La and d) Nb (PEC corrected) compared with lava and bulk tephra (blue shaded region; Clynne, 2011). Panels c) and d) exclude MI with elevated Li and Pb (Supplementary Fig. 3), enrichments indicative of crustal contamination. Fractionation curves calculated using Petrolog 3.1. for MgO and the modal batch melting equation for trace elements for olivine (Ol, solid grey line) and clinopyroxene (CPX, dashed black line) with tick marks which represent 1% fractionation. Partition coefficients were taken from Paster et al. (1974); Sc, CPX-basalt), Beattie, 1994 (Sc, basalt-Ol, La, basalt-Ol), Hauri et al. (1994); (Th., basalt-CPX, La, basalt-CPX, and Nb, basalt-CPX), and McKenzie and O'Nions (1991); (Th, basalt-OL, and Nb, basalt-Ol). Average analytical uncertainty designated by symbol it top right corner of each panel. (For interpretation of the references to color in this figure legend, the reader is referred to the web version of this article.)

magma at 4 kbar, which is near the upper end of trapping pressures estimated from the corrected CO_2 and H_2O contents (Fig. 6). Olivine is predicted to be the liquidus phase for the primitive batch 1 composition, but olivine crystallization alone cannot account for the observed decrease in CaO with decreasing MgO (Fig. 5). Because these basaltic magmas are ultimately derived from the mantle, they may have fractionated olivine and clinopyroxene prior to ascent. Pressures near the Moho beneath the southern Cascades are ~10 kbar (~38 km; Mooney and Weaver, 1989), a pressure above which clinopyroxene may replace olivine as the liquidus phase in hydrous primitive basalts (e.g., Blatter et al., 2013). Mass balance modeling suggests that ~5% high-pressure clinopyroxene fractionation may explain the observed major element differences between the two units (Fig. 5). However, phase equilibrium calculations with pMELTS at 10 kbar for the composition of the early erupted magmas do not predict clinopyroxene as the liquidus phase, so we test this possibility further using the trace element compositions of the uncontaminated MI. Using equilibrium crystallization and partition coefficients between clinopyroxene and basaltic melt for La, Nb, Sc and Th, we model the change in melt composition as the result of clinopyroxene fractionation. Sc is compatible and should decrease rapidly in the melt (Fig. 9a), whereas Nb, Th, and La are incompatible, and should increase slightly (Fig. 9 b, c, d). Comparison with our data shows that 5% clinopyroxene can explain the variability in Sc and the relatively constant Th concentrations in early and late erupted units (Fig. 9a). However, the magnitude of Nb and La increases with decreasing MgO cannot be explained by fractionation alone. Although small amounts of high-pressure clinopyroxene fractionation could have affected the compositions of batch 2 parental magmas, even this process cannot account entirely for the differences in trace element abundances. Our inability to explain the entire trace element variation by fractionation, either in the mantle or in the crust, suggests that their differences may be the result of mantle processes, such as variability in mantle source composition or the degree of partial melting.

Compositional variability among olivine phenocrysts can further be used to distinguish between early and late erupted parental magmas. Fig. 3 compares olivine Ni and Fo core compositions between early and late erupted units. Early erupted LCC-9 has olivine phenocryst cores with high Fo and a restricted range in Ni that requires <1% olivine fractionation. Late erupted olivine cores, in contrast, follow a steep fractionation path (~2–3% olivine fractionation) starting from higher Ni, which may be explained by a slightly more refractory mantle source (e.g., Ruprecht and Plank, 2013).

It is important to note that although magma batches 1 and 2 are geochemically distinct, they are more similar to each other than to most other primitive basaltic magmas in the Lassen region

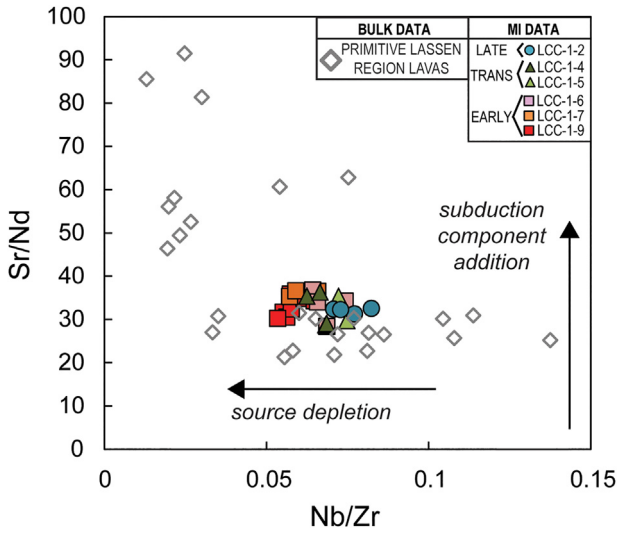

Fig. 10. Comparison of Cinder Cone to Lassen region magmas. PEC corrected MI compositions of Sr/Nd and Nb/Zr (filled colored symbols) compared with other primitive lavas in the Lassen Region (open grey diamonds; Borg et al., 1997). Symbol size for MI exceeds analytical uncertainty. Arrows indicate the relative directions for variability in mantle source depletion and subduction component addition, as labeled.

(Fig. 10; Clynne, 1993; Borg, 1995; Walowski et al., 2015, 2016). Most primitive magmas in the Lassen region are formed by variable additions of slab components to a relatively heterogeneous mantle wedge (Walowski et al., 2015, 2016). Fig. 10 shows similar values of Sr/Nd in early and late erupted magmas that suggest similar amounts of a subduction component. Differences in Nb/Zr, however, suggest that late erupted magma batch 2 may be derived from a slightly less depleted mantle source (Fig. 10). It is also possible that both batches were derived from the same mantle source, but experienced different paths (down-temperature) through the upper-most lithospheric mantle. For example, magma batch 2 may have reacted with lithospheric pyroxenite veins, which could explain the elevated Ni contents in olivine compared to magma batch 1. Regardless of their origin, our data support previous observations that monogenetic cones tap different batches of mantle-derived melts during a single, short-lived eruption (Brenna et al., 2010, 2011; McGee et al., 2011; Rowe et al., 2011). In the Lassen region, specifically, the markedly different mafic compositions erupted (10 different groups of magma) over a short time interval (≤10 ka) at Poison Lake, indicate that mafic magmas can ascend from depth (probably along faults) without much interaction with the crust or each other (Muffler et al., 2011).

6.3. Timescales of storage, mixing and ascent

Olivine phenocrysts from all units have broad, homogeneous cores and Fe-enriched rims (Fig. 11). Nickel concentrations show a similar pattern – homogenous throughout the core, with normal zoning near the rim. While equilibrium between olivine cores and the melt inclusions they host provide evidence that olivine may not necessarily grow as zoned crystals (Danyushevsky et al., 2002), other studies suggest that even small amounts of olivine crystallization lead to measurable changes in surrounding melt composition such that Ni and Fo of the olivine should be normally zoned (e.g., Fig. 11; Straub et al., 2011, Ruprecht and Plank, 2013; Thomson and Maclennan, 2012). Flat cores require some other or an additional process. If the lack of zoning represents a growth process, it requires growth under conditions where Mg/Fe ratios are unchanged during olivine growth. This either implies continuous replenishment of the crystallizing magma body with primitive high Mg# melts or buffering of the melt by growth under high and constant Mg/Fe conditions, such as during crystallization in the mantle (Ruprecht and Plank, 2013). Alternatively, flat cores could be the result of prolonged diffusion that flattens out initial growth zoning (Thomson and Maclennan, 2012). Two different models of initial growth prior to diffusion have emerged, affecting length-scale estimates for potential diffusive equilibration. In addition to the conventional view where crystals grow quasi-concentric from the inside-out with the cores being old and rims young, dendritic rapid growth followed by back-filling and textural equilibration potentially shortens diffusive length-scales (Welsch et al., 2012; Shea et al., 2015).

6.3.1. Pre-eruptive storage timescales

A detailed growth sequence for the Cinder Cone olivine is unknown and therefore one can only calculate a conservative estimate for potential diffusion-related equilibration timescales that would produce flat compositions in olivine cores. Using the scaling relationship $t \sim x^2/D$ derived from Fick's second law, which describes the change in composition with time over a one-dimensional system,

$$\frac{\partial C}{\partial t} = D\frac{\partial^2 C}{\partial x^2} \quad (2)$$

we can estimate to a first order the timescales of olivine residence in a high Mg-Fe melt that equilibrates the entire core. Here C is concentration, t is time, and D is the diffusivity. The above expression of Fick's law assumes a constant diffusion coefficient, D, which for most natural systems is an approximation. The diffusion coefficient for Fe-Mg and Ni in natural olivine, for example, varies with temperature, pressure, oxygen fugacity, composition, and crystallographic orientation (Petry et al., 2004; Dohmen and Chakraborty, 2007). We take the diffusion coefficient along the c-axis, the fast direction, for Ni in olivine as 1.3×10^{-5} μm²/s and for Fe-Mg as 1.14×10^{-5} μm²/s, both calculated for a temperature of 1150 °C (Petry et al., 2004; Dohmen and Chakraborty, 2007, respectively). Flat cores range in size, but are commonly ~300 μm from the center towards the rim (Fig. 11). Applying the scaling relationship to such conditions, we find that cores would need centuries ($t \sim x^2/D_{Ni}$; >200 yr) at high temperature and constant Mg/Fe melt ratios to fully equilibrate. Such storage conditions could occur in either the mantle (Ruprecht and Plank, 2013; Gordeychik et al., 2018) or the crust (Thomson and Maclennan, 2012), as suggested by calculated MI entrapment pressures for the Cinder Cone olivine.

6.3.2. Timescales of mixing and ascent

With respect to the normal zoning near the olivine rims, correlated Fe-Mg and Ni zoning can either reflect new olivine rim growth (e.g. see Fig. 11) or diffusive exchange as a result of mixing between primitive olivine-phyric magmas with more evolved compositions. Ni is compatible in olivine and has a similar diffusivity to Fe-Mg interdiffusion (Petry et al., 2004; Dohmen and Chakraborty, 2007), and therefore follows Fe/Mg in the Cinder Cone olivine phenocrysts (Fig. 11). The Fe-rich and Ni-poor rims were likely developed at the same time as crustal contamination, magma mixing and/or entrainment of olivine in new batches of melt, processes that could lower the Mg and Ni content of the bulk magma. If we assume that the olivine crystals reacted to this change by diffusive re-equilibration, we can use the diffusion time scales of Ni and Fe-Mg to estimate a residence time of olivine in the evolved magma. Although the observed geochemical gradient may be related to new olivine growth, and despite uncertainties related to diffusion coefficients and anisotropy (e.g., Oeser et al., 2018), we aim to utilize the observed relationships to place maximum constraints on mixing and residence timescales and compare with previous studies.

Due to strong diffusion anisotropy in olivine (e.g., Dohmen and Chakraborty, 2007; Shea et al., 2015) we consider only the fast

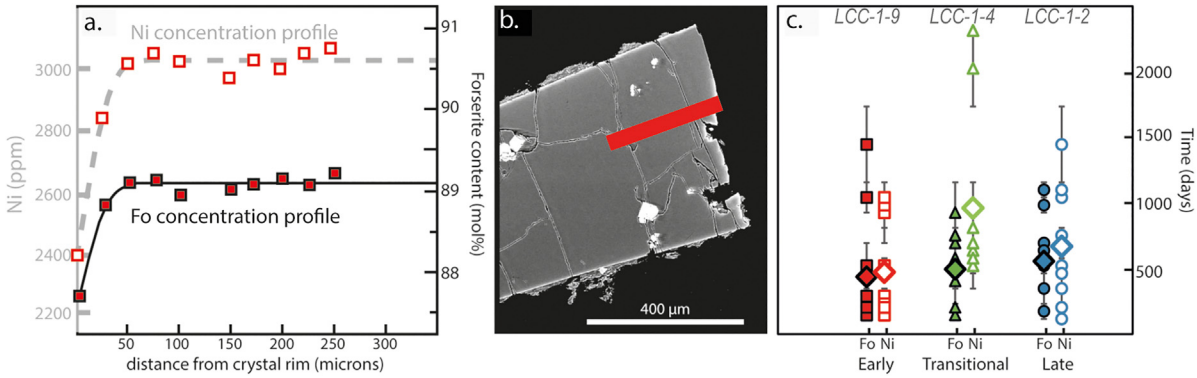

Fig. 11. Complete diffusion model timescale results for Ni (open symbols) and Fo (filled symbols). Points in panel a) representative example of measured core-rim Ni and Fo contents measured by LA-ICP-MS. Panel b) shows a backscatter image of a representative olivine with the location of the laser ablation transect along the c-axis. Panel c) shows timescales (in days) estimated from individual olivine phenocrysts using Ni (open symbols) and Fo (filled symbols) from early from LCC-9 (early erupted; red), LCC-4 (transitional; green), and LCC-2 (late erupted; blue) tephra. Error bars are one standard deviation. (For interpretation of the references to color in this figure legend, the reader is referred to the web version of this article.)

direction along the c-axis, although a rigorous determination of crystallographic axes was not performed, and acknowledge that diffusion along the a and b axes would result in timescales ~6 times slower. For the boundary condition, we assume that the measured Ni and Mg content at the olivine rim is the equilibrium Ni and Mg content of the olivine coexisting with the melt surrounding each olivine crystal. We also assume that the average core composition is representative of the initial olivine core composition before magmatic evolution (Fig. 11).

Using this simple method, we find the olivine phenocrysts record residence times of 0.4–6.3 years (Fig. 11). The average Ni and Fe-Mg diffusion timescales for early and late erupted units are similar at ~500 days (~16 months), and most crystals record times of <~1000 days (Fig. 11c). The uncertainty in these results is derived from choice in temperature, and thus, diffusivity, as well as an inability to determine growth vs. diffusion processes. Petrolog 3.1 estimates average trapping temperatures of ~1150 °C and pre-eruptive temperatures of ~1050 °C. This indicates that temperatures were decreasing during mixing and ascent, which is not captured by our model of the rim zones. Decreasing the temperature would cause an increase in estimated times; however, simultaneous olivine growth would act to significantly decrease this estimated timescale.

Despite the inherent uncertainties and limits of the diffusion chronometry performed here, the calculated olivine residence times at Cinder Cone recorded in the crystal rims are similar to those calculated for olivine from the 18th century eruption of Vólcan Jorullo in central Mexico utilizing similar modeling methods (200 to >1000 days; Johnson et al., 2008). This similarity is interesting given the total length of the Jorullo eruption (≤15 years; Luhr and Carmichael, 1985) was longer than the eruption of Cinder Cone (<5 years; Sheppard et al., 2009). Similarities in the estimated timescales between mixing and storage durations at Cinder Cone and Jorullo emphasize the difference between pre-eruptive timescales of magma assembly compared to the timescales of *syn*-eruptive magma migration and eruption.

6.4. Eruption dynamics

The stratigraphic record and physical characteristics of the same Cinder Cone tephra sample locality from which the olivine-hosted melt inclusions are derived shows that the eruption exhibited two main and distinct eruptive phases (Marks, 2012). Early erupted units LCC-1-9, LCC-1-8, LCC-1-7, LCC-1-6, are dominated by relatively large, highly vesicular golden tephra clasts (Fig. 2), have a restricted area (~40 km^2 for the 5-cm isopach), and componentry characteristics suggestive of a primarily Strombolian eruptive style (Marks, 2012). The late erupted tephra units (LCC-1-4 through LCC-1-1) are markedly finer grained (Fig. 2), have a larger areal extent (~100 km^2 for the 5-cm isopach) and volume, and have tephra componentry analogous to other violent Strombolian cinder cone eruptions (Marks, 2012). The tephra unit LCC-1-4, in particular, is uniquely dominated by dense microcrystalline clasts, and LCC-1-5 is a dark fine ash layer (Fig. 2), interpreted as a transitional unit.

The MI compositions suggest that these two identified explosive phases also correlate with the eruption of two separate magmas tapped during the eruption. This is perhaps surprising, because the volatile concentrations of the two magmas are nearly indistinguishable, with only transitional magmas clearly sampling shallowly degassed compositions. Thus, differences in volatiles alone cannot explain the change in eruptive dynamics observed at Cinder Cone. We therefore suggest that evolution of the subvolcanic magmatic system must have contributed to the change in eruptive style.

The inferred eruption dynamics at Cinder Cone may be analogous to those observed during the April–October 2010 eruption of Eyjafjallajökull. During this Icelandic eruption, the locations of sub-surface seismic events suggest that magma was tapped from new storage reservoirs located at progressively greater depths over the course of the eruption (Tarasewicz et al., 2012). Compositional changes over the course of a single eruption are also observed at Sand Mountain in the central Oregon Cascades, although in this case changes in magma composition were associated with vent migration. These previous observations provide evidence that eruption of an initial magma batch can destabilize other local magma storage reservoirs during a single eruptive episode. Such observations indicate that individual 'monogenetic' eruptions could tap multiple crustal magma lenses. We draw on this analogy to link the petrologic data from Cinder Cone tephra to the eruption dynamics. The most important observations are (1) the volatile contents of olivine-hosted MIs are similar in early and late erupted tephra, despite small compositional differences, (2) olivine diffusion time scales suggest that, on average, olivine crystals spent several months re-equilibrating with a cooler magma prior to eruption and (3) the second main eruptive phase (Unit 3) was more voluminous and more explosive (as measured by grain size and deposit extent) than the first main phase (Unit 2).

These data provide a framework in which to infer the pre-eruptive history of the Cinder Cone magmas. The distinct compositional signatures of the two magma batches require them to be isolated from each other. While the total erupted volume of the first magma batch was small (~0.06 km^3), we suggest that it critically established a connection between the surface and a deeper magma

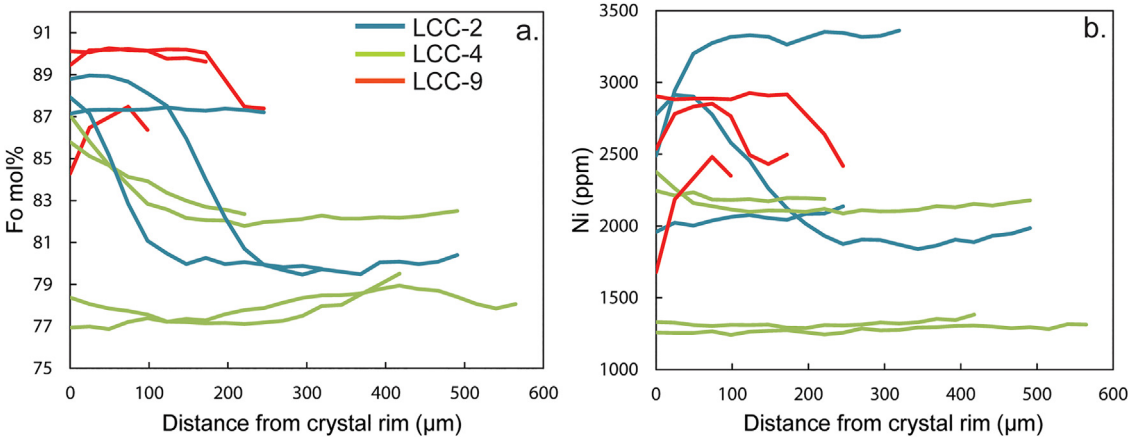

Fig. 12. Core to rim variations in olivine identified as xenocrysts from LCC-9 (early erupted; red), LCC-4 (transitional; green), and LCC-2 (late erupted; blue) tephra, measured by LA-ICP-MS as described in Section 4.2 Analytical Procedures. Diffusion chronometry was not performed on these xenocrysts. (For interpretation of the references to color in this figure legend, the reader is referred to the web version of this article.)

storage region. Magma withdrawal could have depressurized this deeper region, and ultimately destabilized an adjacent vertically extensive magma batch (Unit 3). In effect, we envision the initial conduit as acting like a siphon, such that a lateral pressure gradient at depth drives the second, more explosive, eruption. A similar pattern was seen at Parícutin, where arrival of a new magma batch after the first month of eruptive activity and the changes in cone architecture increased the explosivity and created the largest volume of tephra deposits (Pioli et al., 2008; Pioli et al., 2009). This scenario is also consistent with the hypothesis that the explosivity of hydrous mafic magmas may be more a reflection of driving pressure, which in part controls ascent rate, than of vesiculation kinetics (Cashman and Giordano, 2014).

6.5. *Mechanisms of crustal contamination and plumbing system evolution*

Although the contribution of crustal contamination to the composition of erupted magmas at Cinder Cone is clear, the mechanism by which this contamination occurred is more difficult to decipher. Determining how contamination occurred can provide constraints on how the magmatic plumbing system evolved prior to and during eruption. We suggest two main hypotheses may be used to explain the contamination of the Cinder Cone magmas: 1) A shallow, strongly contaminated batch of magma, perhaps andesitic, was mobilized by and mixed with new batches of magma coming from depth, or 2) an initial batch of magma thermally pre-conditioned the granite, creating a zone of crystal-rich rhyolitic mush that was quickly incorporated into the rising new primitive magma batches. In hypothesis (2), there is no intermediate magma.

The temporal evolution of the SiO_2 contents of the erupted tephra (Clynne, 2011) show that for both main eruptive phases, early magmas are more evolved (basaltic andesite to andesite), and become progressively less evolved over time. These temporal patterns in magma composition are similar to those observed during eruptive episodes 2–47 of Pu'u'O'o in Hawaii (Garcia et al., 1992; Wallace and Anderson Jr, 1998), and may indicate that a shallow, evolved magma batch was simultaneously mixed with and pushed out of the conduit system by the ascending mafic magma, supporting hypothesis 1. Mineralogical or textural evidence for a distinct or separate evolved magma batch, however, seems to be lacking. Olivine xenocrysts with lower-Fo cores may be representative of the shallowly stored evolved magma. However, some of these xenocrystic olivine display low-Fo cores and high-Fo shoulders (Costa and Dungan, 2005), as well as low-Ni cores, high-Ni shoulders, and normally zoned rims, that indicate partial equilibration with the primitive parental magma before crustal contamination occurred (Fig. 12).

Two xenocrysts from transitional unit LCC-4 do not have high-Fo rims, and have significantly lower Fo contents than the other xenocrysts, and may be representative of the mixed magma (Fig. 12). However, it seems likely that these crystals grew in the contaminated magma during an eruptive pause: first, they are only observed in the transitional unit, LCC-4 and second, these samples also show abundant microlite crystallization indicative of temporary shallow magma storage (Marks, 2012). In addition, although none of the analyzed MI have low-Fo olivine hosts, we did not analyze olivine crystals smaller than 250 μm in diameter; there could be a population of low-Fo olivine derived from the contaminated magma in this size fraction.

Strong support for hypothesis (2) lies in the observation that both lava and bulk tephra compositions fall on mixing trajectories between the granitic material and the two parental magma batches. If, for example, magma batch 2 evolved as the result of mixing with the first batch of contaminated erupted magma, one would expect mixing trajectories between magma batch 2 and the contaminated magma of early erupted units, which is not observed.

Using the combined observations presented above, we suggest the following model for plumbing system evolution at Cinder Cone. First, one or several intrusions of batch 2 magma enter the middle crust and form a set of small sills, which may be partially integrated, over a range of depths. In a manner analogous to the model proposed for Burnt Lava Flow (Medicine Lake, CA), which involves the separation of heat and mass transfer (Grove et al., 1988), the crustal sills quench on their margins, and become mechanically separated from the surrounding granitic basement. However, the sills may transfer heat to the surrounding granitic wall rocks; this allows variable degrees of melting, assimilation and contamination, as seen in the MI with contaminated compositions and lower trapping pressures. Some of the low Fo, unzoned xenocrysts (Fig. 12) may be sourced from various parts of this sill complex.

We suggest that batch 1 magma probably ascended to the pre-eruptive storage region shortly after the formation of batch 2. Most of batch 1 magma probably stalled when it interacted with the partially melted granite, mixing and developing zoned rims. That batch 1 magma did not interact directly with batch 2 magma is indicated by the absence of evidence for mixing. After mixing and at least partial equilibration, it appears that the shallow part of the system became destabilized and eventually erupted, with the most heavily contaminated magma erupting first. The diffusion data suggest

that this process occurred over less than one year, well within the timescales often observed for pre-eruptive volcanic unrest. As a result, the batch 2 sills also become destabilized, causing them to ascend, interact with heated and partially molten granite, developing lower Fo rims, and finally erupt in a similar manner to the previously erupted batch 1 magmas.

Although Unit 1 tephra was not sampled in this study, previous work suggests that the Unit 1 eruptive cycle is similar to the others (Unit 2 and 3), but much less voluminous (Heiken, 1978). Thus, this initial magma batch may have served as the trigger for the two main two eruptive cycles, which progressed as described above.

7. Conclusions

The eruption of Cinder Cone produced a series of tephra deposits and lava flows that display complex changes in chemistry over the course of the eruption. High-Fo olivine phenocrysts from all erupted units contain MI that are more primitive in composition than the erupted material. The evolved compositions of the lava and bulk tephra and the abundance of quartz xenocrysts within the deposits suggest the parental magmas were contaminated by granitic material in the middle to upper crust. The basaltic parental magmas sampled by the MI crystallized at minimum depths of ~2.4–4.8 kbar, which equates to approximately 9–18 km below the surface. Distinct compositional variability between early and late erupted units suggest two different mantle-derived basaltic magmas were tapped during the eruption. These two basaltic compositions correlate with the two main explosive phases of the eruption, and were separated by an eruptive slowing or pause evidenced by textural analyses of tephra clasts (Marks, 2012). Diffusion modeling of Ni and Fe-Mg exchange gradients in olivine rims suggests that olivine residence times in an evolving magma were less than years, similar to those calculated for longer-lived scoria cone eruptions, such as Jorullo in Mexico. Temporal changes in lava and bulk tephra compositions indicate that the granitic material was heterogeneously incorporated after olivine growth and MI entrapment. Although the geochemical evidence suggests that the parental magmas were contaminated by either a shallowly stored evolved magma or a granitic mush, the exact mechanisms that drove crustal contamination of the Cinder Cone magmas remain enigmatic. Our combined results provide new insight into the complexities of short-lived monogenetic eruptions.

Acknowledgements

We thank Adam Kent for assistance with LA-ICP-MS measurements and John Donovan for assistance with EPMA. Funding was provided by the National Science Foundation (EAR-1119224 and EAR-1019848). PR also acknowledges support from the National Science Foundation (EAR-1719687).

Appendix A. Supplementary data

Supplementary data to this article can be found online at https://doi.org/10.1016/j.jvolgeores.2019.106665.

References

Aster, E.M., Wallace, P.J., Moore, L.R., Watkins, J., Gazel, E., Bodnar, R.J., 2016. Reconstructing CO_2 concentrations in basaltic melt inclusions using Raman analysis of vapor bubbles. J. Volcanol. Geotherm. Res. 323, 148–162.

Beattie, P., 1994. Systematics and energetics of trace-element partitioning between olivine and silicate melts: implications for the nature of mineral/melt partitioning. Chem. Geol. 117, 57–71.

Berge, P.A., Stauber, D.A., 1987. Seismic refraction study of upper crustal structure in the Lassen Peak Area, northern California. J. Geophys. Res. Solid Earth 92, 10571–10579.

Blatter, D.L., Sisson, T.W., Hankins, W.B., 2013. Crystallization of oxidized, moderately hydrous arc basalt at mid-to lower-crustal pressures: implications for andesite genesis. Contrib. Mineral. Petrol. 166, 861–886.

Borg, L.E., 1995. The Origin and Evolution of Magmas from the Lassen Region of the Southernmost Cascades. University of Texas at Austin.

Borg, L.E., Clynne, M.A., Bullen, T.D., 1997. The variable role of slab-derived fluids in the generation of a suite of primitive calc-alkaline lavas from the southernmost Cascades, California. Can. Mineral. 35, 425–452.

Borg, L.E., Blichert-Toft, J., Clynne, M.A., 2002. Ancient and modern subduction zone contributions to the mantle sources of lavas from the Lassen region of California inferred from Lu–Hf isotopic systematics. J. Petrol. 43, 705–723.

Brenna, M., Cronin, S.J., Smith, I.E., Sohn, Y.K., Németh, K., 2010. Mechanisms driving polymagmatic activity at a monogenetic volcano, Udo, Jeju Island, South Korea. Contrib. Mineral. Petrol. 160, 931–950.

Brenna, M., Cronin, S.J., Nemeth, K., Smith, I.E., Sohn, Y.K., 2011. The influence of magma plumbing complexity on monogenetic eruptions, Jeju Island, Korea. Terra Nova 23, 70–75.

Bucholz, C.E., Gaetani, G.A., Behn, M.D., Shimizu, N., 2013. Post-entrapment modification of volatiles and oxygen fugacity in olivine-hosted melt inclusions. Earth Planet. Sci. Lett. 374, 145–155.

Cashman, K.V., Giordano, G., 2014. Calderas and magma reservoirs. J. Volcanol. Geotherm. Res. 288, 28–45.

Cecil, M.R., Rotberg, G.L., Ducea, M.N., Saleeby, J.B., Gehrels, G.E., 2012. Magmatic growth and batholithic root development in the northern Sierra Nevada, California. Geosphere 8, 592–606.

Clynne, M.A., 1993. Geologic Studies of the Lassen Volcanic Center, Cascade Range, California. University of California, Santa Cruz (Unpublished Dissertation).

Clynne, M.A., 2011. Stratigraphy and compositional evolution of Cinder Cone, a composite monogenetic cone in Lassen Volcanic National Park, California. AGU Fall Meeting Abstracts vol. 1, 2621.

Clynne, M.A., Muffler, L.J.P., 2010. Geologic Map of Lassen Volcanic National Park and Vicinity, California. US Department of the Interior, US Geological Survey.

Clynne, M. A., Champion, D. E., Trimble, D. A., Hendley II J. W., & Stauffer, P. H. (2000). How Old IsĈinder Cone? Solving a Mystery in Lassen Volcanic National Park, California (No. 023–00). US Geological Survey.

Costa, F., Dungan, M., 2005. Short time scales of magmatic assimilation from diffusion modeling of multiple elements in olivine. Geology 33 (10), 837–840.

Costa, F., Morgan, D., 2011. Time constraints from chemical equilibration in magmatic crystals. In: Timescales of Magmatic Processes: From Core to Atmosphere. Wiley, Chichester, pp. 125–159.

Danyushevsky, L.V., 2001. The effect of small amounts of H_2O on crystallisation of mid-ocean ridge and backarc basin magmas. J. Volcanol. Geotherm. Res. 110 (3), 265–280.

Danyushevsky, L.V., Plechov, P., 2011. Petrolog3: Integrated software for modeling crystallization processes. Geochem. Geophys. Geosyst. (17), 12.

Danyushevsky, L.V., Della-Pasqua, F.N., Sokolov, S., 2000. Re-equilibration of melt inclusions trapped by magnesian olivine phenocrysts from subduction-related magmas: petrological implications. Contrib. Mineral. Petrol. 138, 68–83.

Danyushevsky, L.V., Sokolov, S., Falloon, T.J., 2002. Melt inclusions in olivine phenocrysts: using diffusive re-equilibration to determine the cooling history of a crystal, with implications for the origin of olivine-phyric volcanic rocks. J. Petrol. 43 (9), 1651–1671.

Dixon, J.E., Pan, V., 1995. Determination of the molar absorptivity of dissolved carbonate in basanitic glass. Am. Mineral. 80, 1339–1342.

Dixon, J.E., Stolper, E.M., Holloway, J.R., 1995. An experimental study of water and carbon dioxide solubilities in mid-ocean ridge basaltic liquids. Part I: calibration and solubility models. J. Petrol. 36 (6), 1607–1631.

Dohmen, R., Chakraborty, S., 2007. Fe–Mg diffusion in olivine II: point defect chemistry, change of diffusion mechanisms and a model for calculation of diffusion coefficients in natural olivine. Phys. Chem. Miner. 34, 409–430.

Erlund, E.J., Cashman, K.V., Wallace, P.J., Pioli, L., Rosi, M., Johnson, E., Granados, H.D., 2010. Compositional evolution of magma from Parícutin Volcano, Mexico: the tephra record. J. Volcanol. Geotherm. Res. 197, 167–187.

Esposito, R., Bodnar, R.J., Danyushevsky, L.V., De Vivo, B., Fedele, L., Hunter, J., Shimizu, N., 2011. Volatile evolution of magma associated with the Solchiaro eruption in the Phlegrean volcanic district (Italy). J. Petrol. 52, 2431–2460.

Gaetani, G.A., Grove, T.L., 1998. The influence of water on melting of mantle peridotite. Contrib. Mineral. Petrol. 131, 323–346.

Gaetani, G.A., O'Leary, J.A., Shimizu, N., Bucholz, C.E., Newville, M., 2012. Rapid reequilibration of H2O and oxygen fugacity in olivine-hosted melt inclusions. Geology 40, 915–918.

Garcia, M.O., Rhodes, J.M., Wolfe, E.W., Ulrich, G.E., Ho, R.A., 1992. Petrology of lavas from episodes 2–47 of the Pu'u' O'o eruption of Kilauea Volcano, Hawaii: evaluation of magmatic processes. Bull. Volcanol. 55 (1–2), 1–16.

Ghiorso, M.S., Gualda, G.A., 2015. An H 2 O–CO 2 mixed fluid saturation model compatible with rhyolite-MELTS. Contrib. Mineral. Petrol. 169 (6), 53.

Ghiorso, M.S., Hirschmann, M.M., Reiners, P.W., Kress, V.C., 2002. The pMELTS: a revision of MELTS for improved calculation of phase relations and major element partitioning related to partial melting of the mantle to 3 GPa. Geochem. Geophys. Geosyst. 3, 1–35.

Gordeychik, B., Churikova, T., Kronz, A., Sundermeyer, C., Simakin, A., Wörner, G., 2018. Growth of, and diffusion in, olivine in ultra-fast ascending basalt magmas from Shiveluch volcano. Sci. Rep. 8 (1), 11775.

Grove, T.L., Kinzler, R.J., Baker, M.B., Donnelly-Nolan, J.M., Lesher, C.E., 1988. Assimilation of granite by basaltic magma at Burnt Lava flow, Medicine Lake volcano,

northern California: decoupling of heat and mass transfer. Contrib. Mineral. Petrol. 99, 320–343.
Grove, T.L., Chatterjee, N., Parman, S.W., Médard, E., 2006. The influence of H2O on mantle wedge melting. Earth Planet. Sci. Lett. 249, 74–89.
Gualda, G.A., Ghiorso, M.S., Lemons, R.V., Carley, T.L., 2012. Rhyolite-MELTS: a modified calibration of MELTS optimized for silica-rich, fluid-bearing magmatic systems. J. Petrol. 53, 875–890.
Hartley, M.E., Maclennan, J., Edmonds, M., Thordarson, T., 2014. Reconstructing the deep CO_2 degassing behaviour of large basaltic fissure eruptions. Earth Planet. Sci. Lett. 393, 120–131.
Hauri, E.H., Wagner, T.P., Grove, T.L., 1994. Experimental and natural partitioning of Th, U, Pb and other trace elements between garnet, clinopyroxene and basaltic melts. Chem. Geol. 117, 149–166.
Heiken, G., 1978. Characteristics of tephra from Cinder Cone, Lassen volcanic national park, California. Bull. Volcanol. 41, 119–130.
Hirschmann, M.M., Tenner, T., Aubaud, C., Withers, A.C., 2009. Dehydration melting of nominally anhydrous mantle: the primacy of partitioning. Phys. Earth Planet. Inter. 176, 54–68.
Holloway, J.R., Blank, J.G., 1994. Application of experimental results to COH species in natural melts. Rev. Mineral. Geochem. 30, 187–230.
Iacono-Marziano, G., Morizet, Y., Le Trong, E., Gaillard, F., 2012. New experimental data and semi-empirical parameterization of H2O–CO2 solubility in mafic melts. Geochim. Cosmochim. Acta 97, 1–23.
Johnson, E.R., Wallace, P.J., Cashman, K.V., Granados, H.D., Kent, A.J., 2008. Magmatic volatile contents and degassing-induced crystallization at Volcán Jorullo, Mexico: implications for melt evolution and the plumbing systems of monogenetic volcanoes. Earth Planet. Sci. Lett. 269, 478–487.
Johnson, E.R., Wallace, P.J., Delgado Granados, H., Manea, V.C., Kent, A.J., Bindeman, I.N., Donegan, C.S., 2009. Subduction-related volatile recycling and magma generation beneath Central Mexico: insights from melt inclusions, oxygen isotopes and geodynamic models. J. Petrol. 50 (9), 1729–1764.
Johnson, E.R., Wallace, P.J., Cashman, K.V., Granados, H.D., 2010. Degassing of volatiles (H2O, CO2, S, Cl) during ascent, crystallization, and eruption at mafic monogenetic volcanoes in central Mexico. J. Volcanol. Geotherm. Res. 197, 225–238.
Kumazawa, M., Anderson, O.L., 1969. Elastic moduli, pressure derivatives, and temperature derivatives of single-crystal olivine and single-crystal forsterite. J. Geophys. Res. 74 (25), 5961–5972.
Lange, R.L., Carmichael, I.S., 1990. Thermodynamic properties of silicate liquids with emphasis on density, thermal expansion and compressibility. Rev. Mineral. Geochem. 24, 25–64.
Le Bas, M.J., Le Maitre, R.W., Streckeisen, A., Zanettin, B., 1986. A chemical classification of volcanic rocks based on the total alkali-silica diagram. J. Petrol. 27, 745–750.
Le Roux, V., Dasgupta, R., Lee, C.T., 2011. Mineralogical heterogeneities in the Earth's mantle: Constraints from Mn, Co, Ni and Zn partitioning during partial melting. Earth Planet. Sci. Lett. 307 (3), 395–408.
Le Voyer, M., Rose-Koga, E.F., Shimizu, N., Grove, T.L., Schiano, P., 2010. Two contrasting H2O-rich components in primary melt inclusions from Mount Shasta. J. Petrol. 51, 1571–1595.
Leeman, W.P., Tonarini, S., Chan, L.H., Borg, L.E., 2004. Boron and lithium isotopic variations in a hot subduction zone—the southern Washington Cascades. Chem. Geol. 212 (1), 101–124.
Lloyd, A.S., Plank, T., Ruprecht, P., Hauri, E.H., Rose, W., 2013. Volatile loss from melt inclusions in pyroclasts of differing sizes. Contrib. Mineral. Petrol. 165, 129–153.
Loewen, M.W., Kent, A.J., 2012. Sources of elemental fractionation and uncertainty during the analysis of semi-volatile metals in silicate glasses using LA-ICP-MS. J. Anal. At. Spectrom. 27, 1502–1508.
Lowenstern, J.B., 1995. Applications of silicate-melt inclusions to the study of magmatic volatiles. Magmas Fluids Ore Deposits 23, 71–99.
Luhr, J.F., 2001. Glass inclusions and melt volatile contents at Parícutin Volcano, Mexico. Contrib. Mineral. Petrol. 142, 261–283.
Luhr, J.F., Carmichael, I.S., 1985. Jorullo Volcano, Michoacán, Mexico (1759–1774): the earliest stages of fractionation in calc-alkaline magmas. Contrib. Mineral. Petrol. 90, 142–161.
Mallmann, G., O'Neill, H.S.C., 2009. The crystal/melt partitioning of V during mantle melting as a function of oxygen fugacity compared with some other elements (Al, P, Ca, Sc, Ti, Cr, Fe, Ga, Y, Zr and Nb). J. Petrol. 50, 1765–1794.
Marks, J.K., 2012. Physical Volcanology of the 1666 C.E. Cinder Cone Eruption, Lassen Volcanic National Park, California. University of Oregon.
McBirney, A.R., Taylor, H.P., Armstrong, R.L., 1987. Parícutin re-examined: a classic example of crustal assimilation in calc-alkaline magma. Contrib. Mineral. Petrol. 95, 4–20.
McGee, L.E., Beier, C., Smith, I.E., Turner, S.P., 2011. Dynamics of melting beneath a small-scale basaltic system: a U-Th–Ra study from Rangitoto volcano, Auckland volcanic field, New Zealand. Contrib. Mineral. Petrol. 162 (3), 547–563.
McKenzie, D.A.N., O'Nions, R.K., 1991. Partial melt distributions from inversion of rare earth element concentrations. J. Petrol. 32, 1021–1091.
Métrich, N., Wallace, P.J., 2008. Volatile abundances in basaltic magmas and their degassing paths tracked by melt inclusions. Rev. Mineral. Geochem. 69, 363–402.
Mooney, W.D., Weaver, C.S., 1989. Regional crustal structure and tectonics of the Pacific coastal states; California, Oregon, and Washington. Geophysical Framework of the Continental United States, 172., pp. 129–161.
Moore, L.R. Gazel, E., Tuohy, R., Lloyd, A., Esposito, R., Steele-MacInnis, M., Hauri, E.H., Wallace, P.J., Plank, T., Bodnar, R.J. (2014). Bubbles matter: an assessment of the contribution of vapor bubbles to melt inclusion volatile budgets. Am. Mineral., in press.
Muffler, L.J.P., Clynne, M.A., Calvert, A.T., Champion, D.E., 2011. Diverse, discrete, mantle-derived batches of basalt erupted along a short normal fault zone: The Poison Lake chain, southernmost Cascades. Bulletin 123 (11-12), 2177–2200.
Newman, S., Lowenstern, J.B., 2002. VolatileCalc: a silicate melt–H2O–CO2 solution model written in Visual basic for Excel. Comput. Geosci. 28, 597–604.
Oeser, M., Ruprecht, P., Weyer, S., 2018. Combined Fe-Mg chemical and isotopic zoning in olivine constraining magma mixing-to-eruption timescales for the continental arc volcano Irazú (Costa Rica) and Cr diffusion in olivine. Am. Miner. J. Earth Planet. Mater. 103 (4), 582–599.
Papale, P., Moretti, R., Barbato, D., 2006. The compositional dependence of the saturation surface of H2O + CO2 fluids in silicate melts. Chem. Geol. 229, 78–95.
Paster, T.P., Schauwecker, D.S., Haskin, L.A., 1974. The behavior of some trace elements during solidification of the Skaergaard layered series. Geochim. Cosmochim. Acta 38, 1549–1577.
Petry, C., Chakraborty, S., Palme, H., 2004. Experimental determination of Ni diffusion coefficients in olivine and their dependence on temperature, composition, oxygen fugacity, and crystallographic orientation. Geochim. Cosmochim. Acta 68, 4179–4188.
Pioli, L., Erlund, E., Johnson, E.R., Cashman, K.V., Wallace, P.J., Rosi, M., Granados, H.D., 2008. Explosive dynamics of violent Strombolian eruptions: the eruption of Parícutin Volcano 1943–1952 (Mexico). Earth Planet. Sci. Lett. 271, 359–368.
Pioli, L., Azzopardi, B.J., Cashman, K.V., 2009. Controls on the explosivity of scoria cone eruptions: Magma segregation at conduit junctions. J. Volcanol. Geotherm. Res. 186 (3–4), 407–415.
Riker, J., Unpublished M.S. Thesis 2005. The 1859 Eruption of Mauna Loa Volcano, Hawaii: Controls on the Development of Long Lava Channels. University of Oregon.
Roedder, E., 1979. Origin and significance of magmatic inclusions. Bull. Mineral. 102 (5), 487–510.
Roggensack, K., Hervig, R.L., McKnight, S.B., Williams, S.N., 1997. Explosive basaltic volcanism from Cerro Negro volcano: influence of volatiles on eruptive style. Science 277, 1639–1642.
Rowe, M.C., Peate, D.W., Ukstins Peate, I., 2011. An investigation into the nature of the magmatic plumbing system at Parícutin Volcano, Mexico. J. Petrol. 52 (11), 2187–2220.
Ruprecht, P., Plank, T., 2013. Feeding andesitic eruptions with a high-speed connection from the mantle. Nature 500, 68–72.
Ruscitto, D.M., Wallace, P.J., Johnson, E.R., Kent, A.J.R., Bindeman, I.N., 2010. Volatile contents of mafic magmas from cinder cones in the Central Oregon High Cascades: Implications for magma formation and mantle conditions in a hot arc. Earth Planet. Sci. Lett. 298, 153–161.
Ruscitto, D.M., Wallace, P.J., Kent, A.J.R., 2011. Revisiting the compositions and volatile contents of olivine-hosted melt inclusions from the Mount Shasta region: implications for the formation of high-Mg andesites. Contrib. Mineral. Petrol. 162, 109–132.
Saleeby, J.B., Shaw, H.F., Niemeyer, S., Moores, E.M., Edelman, S.H., 1989. U/Pb, Sm/Nd and Rb/Sr geochronological and isotopic study of northern Sierra Nevada ophiolitic assemblages, California. Contrib. Mineral. Petrol. 102, 205–220.
Shea, T., Lynn, K.J., Garcia, M.O., 2015. Cracking the olivine zoning code: Distinguishing between crystal growth and diffusion. Geology 43 (10), 935–938.
Sheppard, P.R., Ort, M.H., Anderson, K.C., Clynne, M.A., May, E.M., 2009. Multiple dendrochronological responses to the eruption of Cinder Cone, Lassen Volcanic National Park, California. Dendrochronologia 27, 213–221.
Sobolev, A.V., Hofmann, A.W., Sobolev, S.V., Nikogosian, I.K., 2005. An olivine-free mantle source of Hawaiian shield basalts. Nature 434 (7033), 590–597.
Straub, S.M., Gomez-Tuena, A., Stuart, F.M., Zellmer, G.F., Espinasa-Perena, R., Cai, Y., Iizuka, Y., 2011. Formation of hybrid arc andesites beneath thick continental crust. Earth Planet. Sci. Lett. 303 (3), 337–347.
Sun, S.S., McDonough, W.F., 1989. Chemical and isotopic systematics of oceanic basalts: implications for mantle composition and processes. Geol. Soc. Lond., Spec. Publ. 42 (1), 313–345.
Suzuki, I., 1975. Thermal expansion of periclase and olivine, and their anharmonic properties. J. Phys. Earth 23 (2), 145–159.
Tarasewicz, J., Brandsdóttir, B., White, R.S., Hensch, M., Thorbjarnardóttir, B., 2012. Using microearthquakes to track repeated magma intrusions beneath the Eyjafjallajökull stratovolcano, Iceland. Journal of Geophysical Research: Solid Earth 117 (B9).
Thomson, A., Maclennan, J., 2012. The distribution of olivine compositions in Icelandic basalts and picrites. J. Petrol. 54 (4), 745–768.
Tuohy, R.M., Wallace, P.J., Loewen, M.W., Swanson, D.A., Kent, A.J., 2016. Magma transport and olivine crystallization depths in Kīlauea's east rift zone inferred from experimentally rehomogenized melt inclusions. Geochim. Cosmochim. Acta 185, 232–250.
Wallace, P.J., Anderson Jr., A.T., 1998. Effects of eruption and lava drainback on the H_2O contents of basaltic magmas at Kilauea Volcano. Bull. Volcanol. 59 (5), 327–344.
Wallace, P.J., Kamenetsky, V.S., Cervantes, P., 2015. Melt inclusion CO_2 contents, pressures of olivine crystallization, and the problem of shrinkage bubbles. Am. Mineral. 100, 787–794.
Walowski, K.J., Wallace, P.J., Hauri, E.H., Wada, I., Clynne, M.A., 2015. Slab melting beneath the Cascade Arc driven by dehydration of altered oceanic peridotite. Nat. Geosci. 8, 404–408.

Walowski, K.J., Wallace, P.J., Clynne, M.A., Rasmussen, D.J., Weis, D., 2016. Slab melting and magma formation beneath the southern Cascade arc. Earth Planet. Sci. Lett. 446, 100–112.
Welsch, B., Faure, F., Famin, V., Baronnet, A., Bachèlery, P., 2012. Dendritic crystallization: a single process for all the textures of olivine in basalts? J. Petrol. 54 (3), 539–574.
Wilcox, R.E., 1954. Petrology of Paricutín volcano Mexico (No. 965). US Government Printing Office.
Wood, C.A., 1980. Morphometric analysis of cinder cone degradation. J. Volcanol. Geotherm. Res. 8 (2–4), 137–160.